

A. AN AB INITIO STUDY OF $\text{Li}_2[\text{CO}_3]$
AND $\text{Na}_2[\text{CO}_3]$ ION TRIPLETS

B. THEORETICAL STUDIES OF TUNNELING PROCESSES
IN THREE-BODY EXCHANGE REACTIONS
OF VAN DER WAALS RARE
GAS DIMERS

By

RANDY ALLEN TURNER

Bachelor of Science

Baylor University

Waco, Texas

1980

Submitted to the Faculty of the
Graduate College of the
Oklahoma State University
in partial fulfillment of
the requirements for
the Degree of
MASTER OF SCIENCE
May, 1990

Thesis

1990

T9514

A. AN AB INITIO STUDY OF $\text{Li}_2[\text{CO}_3]$

AND $\text{Na}_2[\text{CO}_3]$ ION TRIPLETS

B. THEORETICAL STUDIES OF TUNNELING PROCESSES

IN THREE-BODY EXCHANGE REACTIONS

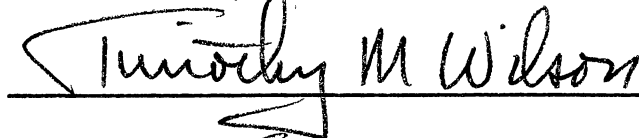
OF VAN DER WAALS RARE

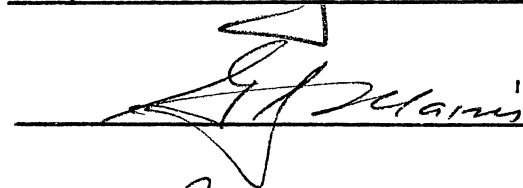
GAS DIMERS

Thesis Approved:



Thesis Advisor







Dean of the Graduate College

ACKNOWLEDGEMENTS

It has been said that no man is an island. Scientific research is truly a group effort that transcends the efforts of any one individual. I wish to thank those who have helped my endeavors.

I wish to give special thanks to my research advisor, Dr. J. Paul Devlin, for his help, his insights, his encouragement, and most of all his understanding during my tenure at Oklahoma State University. I wish to thank the members of my committee, Dr. T. M. Wilson for his support and suggestions, and Dr. G. J. Mains for his uncanny ability to see all things clearly, be they in science or in life.

For my parents, Maj. Edward and Juanita Turner, who had the patience to guide my younger years so that I would develop a love of life and a zest for knowledge, it has been a long time coming. I hope to make you proud.

And to Dr. Joy R. Steidl, for her unshakable belief in me, goes the rest of my life.

TABLE OF CONTENTS

Part A. AN AB INITIO STUDY OF $\text{Li}_2[\text{CO}_3]$ and $\text{Na}_2[\text{CO}_3]$ ION TRIPLETS

Chapter	page
I. INTRODUCTION	1
II. COMPUTATIONAL PROCEDURE	4
III. RESULTS AND DISCUSSION	9
IV. CONCLUSIONS	32
BIBLIOGRAPHY	34

Part B. THEORETICAL STUDIES OF TUNNELING PROCESSES IN THREE-BODY EXCHANGE REACTIONS OF VAN DER WAALS RARE GAS DIMERS

Chapter	page
I. INTRODUCTION	36
II. COMPUTATIONAL PROCEDURE	39
III. RESULTS AND DISCUSSION	45
IV. CONCLUSIONS	70
BIBLIOGRAPHY	71

LIST OF TABLES

Part A.

Table		page
I.	Gaussian Function Exponents and Coefficients for 3-21G Basis Set	7
II.	Gaussian Function Exponents and Coefficients for 4-31G Basis Set	8
III.	Equilibrium Geometries for $[\text{CO}_3]^{2-}$ at 3-21G and 4-31G Levels	10
IV.	Total Electron Densities and Net Charges for $[\text{CO}_3]^{2-}$ at 3-21G and 4-31G Levels .	12
V.	Calculated and Observed Frequencies for $[\text{CO}_3]^{2-}$	13
VI.	Equilibrium Geometry and Restricted Hartree-Fock Energy of $\text{Li}_2[\text{CO}_3]$ at 3-21G Level	14
VII.	Equilibrium Geometry and Restricted Hartree-Fock Energy of $\text{Na}_2[\text{CO}_3]$ at 3-21G Level	15
VIII.	Total Electron Densities and Net Charges for $\text{Li}_2[\text{CO}_3]$ at the 3-21G Level	16
IX.	Total Electron Densities and Net Charges for $\text{Na}_2[\text{CO}_3]$ at the 3-21G Level	17
X.	Calculated Frequencies and Splittings for $\text{Li}_2[\text{CO}_3]$ at 3-21G Level	21
XI.	Calculated Frequencies and Splittings for $\text{Na}_2[\text{CO}_3]$ at 3-21G Level	23
XII.	Calculated and Observed Frequencies for Alkali-metal Carbonates	26

Table	page
-------	------

XIII.	Equilibrium Geometry and Restricted Hartree-Fock energy of $\text{Li}_2[\text{CO}_3]$ at 4-31G Level	27
XIV.	Total Electron Densities and Net Charges for $\text{Li}_2[\text{CO}_3]$ at 4-31G level	28
XV.	Calculated Frequencies and Splittings for $\text{Li}_2[\text{CO}_3]$ at 4-31G Level	29

Part B.

Table	page
-------	------

I.	Pairwise Morse Potential Parameters . . .	40
II.	Exchange Reaction Cross Sections	69

LIST OF FIGURES

Part B.

Figure		page
1.	Plots of the Ne-Ne and Xe-Xe Potential . .	41
2.	Plots of the Ne-Kr Potential for Rotational States	42
3.	Distribution of Lifetimes for Ar_2^*	47
4.	Distributions of Trajectory Lifetimes for KrNe	49
5.	Distributions of Trajectory Lifetimes for KrAr	50
6.	Distributions of WKB Lifetimes for the Kr + NeAr system	52
7.	Distributions of Lifetimes for KrXe . . .	53
8.	Distributions of Lifetimes for KrNe . . .	55
9.	Distributions of Trajectory Lifetimes for XeAr	56
10.	Angular Scattering Distributions for KrAr	57
11.	Angular Scattering Distributions for KrNe	58
12.	Angular Scattering Distributions for XeAr	59
13.	Angular Scattering Distributions for A + BB systems	60
14.	Angular Scattering Distributions for KrNe	63

CHAPTER I

INTRODUCTION

Interest in ion pairs stems from their use as probes of various chemical environments. Distortion of highly symmetric anions, such as NO_3^- , from D_{3h} to some lower symmetry as a result of ion pairing has been extensively researched. Such distortion gives rise to the appearance of new absorption bands in the vibrational spectra. Thus alkali-metal nitrates have been used to determine the structure of aqueous solutions,¹ non-aqueous solutions,² and molten salts.³ The nitrate ion is a particularly useful structural probe; however, there are several other anions with high symmetry and stability which have been useful as well. Alkali-metal chlorates and perchlorates have been particularly useful for studying molten salts.^{4,5} Although the chlorate ion has a C_{3v} symmetry (lower than the nitrate) its vibrational modes are well characterized⁶, and thus the splitting of the vibrational modes when the anion is distorted, are as useful as the splittings of the nitrate ion for determining structure. The

latest use of these ion pair splittings has been for various types of drug analysis.⁷

Many different methods have been used to study ion pairs and their interactions. Experimental methods include high temperature vapor studies, molten salt techniques, mass spectrometric experiments,⁸ and matrix isolation techniques.^{9,10} Even laser mass spectrometry has been used for simultaneous generation and measurement of ion pairs.¹¹

Ab initio methods have also been used to study various ion pairs. The Cambridge Analytic Derivative Package¹² has been used for structural and vibrational frequency calculations for $\text{Li}[\text{NO}_3]$, $\text{Na}[\text{NO}_3]$, $\text{Li}[\text{ClO}_3]$, and $\text{Na}[\text{ClO}_3]$.^{13,14} There has been widespread use of the Gaussian system of programs¹⁵ (revised periodically) for a variety of different calculations, not the least of which are ion pairs.

Singly charged anions are not the only species which have received attention. Anions such as sulfates and carbonates have also been studied extensively. However, the sulfates and carbonates present a unique experimental problem. At elevated temperatures, such as those which might be used to obtain a vapor or a molten salt, the sulfates and carbonates tend to decompose into SO_2 and O_2 or into CO_2 and O_2 , leaving

the elemental alkali-metal and/or alkali-metal oxide.¹⁶ Matrix isolation techniques have been quite useful in overcoming this problem. It has been found that the sulfate anion is not a very good ion probe.¹⁷ Although the proper symmetry requirements are present, the sulfate anion shows only minimal distortion effects. The carbonate anion, however, behaves much like a nitrate anion when it is distorted by associated cations. Excellent experimental data have been produced for the higher alkali-metal carbonates.^{18,19} However, no ab initio calculations have been performed for any of the alkali-metal carbonates. The purpose of this study is the application of ab initio methods to resolve some of the questions about the geometric structures and vibrational frequencies of the carbonates. Although it will not be possible to directly compare the results from this study of the lower alkali-metal carbonates with the experimental data for the higher alkali-metal carbonates, trends will be established in order to link the different sets of data.

CHAPTER II

COMPUTATIONAL PROCEDURE

Ab initio molecular orbital calculations can be performed using any one of several gaussian-type basis sets. These range from simple minimal basis sets where there is only one basis function for each atomic orbital, to more flexible split-valence basis sets in which each valence orbital is represented by two basis functions, to polarization basis sets where functions of higher angular quantum number than are occupied in the atomic ground state are incorporated. While minimal basis sets, such as STO-3G in which least-squares representations of Slater-type orbitals are used,²⁰ and give reasonably good molecular equilibrium geometries, they do not give adequate descriptions of relative energies and force constants.²¹ Split-valence basis sets have atomic functions expressed as fixed linear combinations of Gaussian functions,²² such as

$$gs(\alpha, r) = (2\alpha/\pi)^{3/4} \exp(-\alpha r^2) ,$$

$$gpx(\alpha, r) = (129\alpha^5/\pi^3)^{1/4} \times \exp(-\alpha r^2).$$

Each inner shell is represented by a single basis function written as a sum of K Gaussians, and each valence orbital is split into inner and outer components represented by L and M Gaussians, respectively, where K, L, and M are integers, and these basis sets are denoted as K-LMG. The expansion coefficients and Gaussian exponents are determined by minimizing the total calculated energy of the atomic ground state for each element. Once determined, the entire basis set for each element may be stored and retrieved as needed.

Calculations in this paper were performed using the Gaussian 82 system of basis sets and programs developed at Carnegie-Mellon University.²³ Calculations for $[\text{CO}_3]^{2-}$ and $\text{Na}_2[\text{CO}_3]$ were carried out using the 3-21G split-valence basis set,²⁴ where the inner shell expansions are the combination of three Gaussian functions, the inner component of the valence orbital expansion is a combination of two Gaussian functions, and the outer component of the valence orbital expansion is represented by one Gaussian function. Calculations for $\text{Li}_2[\text{CO}_3]$ were performed using 3-21G and 4-31G split valence basis sets. All equilibrium geometries were fully optimized using numerical gradient methods at the

Hartree-Fock level.²⁵ The resultant optimized geometries were verified using analytical gradient methods, and vibrational frequencies were calculated for each of the molecules using the frequency portion of the Gaussian 82 program. Tables I and II give the program-supplied Gaussian function coefficients used in these calculations. The standard convergence limits employed by the Gaussian 82 program were followed in all calculations.

TABLE I. Gaussian function exponents and coefficients for 3-21G basis set.

Atom	shell type	exponent	s-coefficient	p-coefficient
C	1s	0.172256D+03	0.617669D-01	0.0
		0.259109D+02	0.358794D+00	0.0
		0.553335D+01	0.700713D+00	0.0
	2spI	0.366498D+01	-0.395897D+00	0.236460D+00
		0.770545D+00	0.121584D+01	0.860619D+00
	2spO	0.195857D+00	0.100000D+01	0.100000D+01
Li	1s	0.368382D+02	0.696686D-01	0.0
		0.548172D+01	0.381346D+00	0.0
		0.111327D+01	0.681702D+00	0.0
	2spI	0.540205D+00	-0.263127D+00	0.161546D+00
		0.102255D+00	0.114339D+01	0.915663D+00
	2spO	0.285645D-01	0.100000D+01	0.100000D+01
Na	1s	0.547613D+03	0.674911D-01	0.0
		0.820678D+02	0.393505D+00	0.0
		0.176917D+02	0.665605D+00	0.0
	2sp	0.175407D+02	-0.111937D+00	0.128233D+00
		0.379398D+01	0.254654D+00	0.471533D+00
		0.906441D+00	0.844417D+00	0.604273D+00
	3spI	0.501824D+00	0.219660D+00	0.906649D-02
		0.609458D-01	0.108912D+01	0.997202D+00
	3spO	0.244349D-01	0.100000D+01	0.100000D+01
O	1s	0.322037D+03	0.592394D-01	0.0
		0.484308D+02	0.351500D+00	0.0
		0.104206D+02	0.707658D+00	0.0
	2spI	0.704294D+01	-0.404453D+00	0.244586D+00
		0.157620D+01	0.122156D+01	0.853955D+00
	2spO	0.373684D+00	0.100000D+01	0.100000D+01

TABLE II. Gaussian function exponents and coefficients for 4-31G basis set.

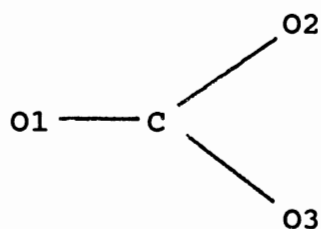
Atom	shell type	exponent	s-coefficient	p-coefficient	
C	1s	0.486967D+03	0.177258D-01	0.0	
		0.733711D+02	0.123478D+00	0.0	
		0.164135D+02	0.433875D+00	0.0	
		0.433498D+02	0.561504D+00	0.0	
	2sp	0.867353D+01	-0.121384D+00	0.635454D-01	
		0.209662D+01	-0.227338D+00	0.298268D+00	
		0.604651D+00	0.118517D+01	0.100000D+01	
	2sp	0.169710D+00	0.100000D+01	0.100000D+01	
	Li	1s	0.275394D+03	0.612185D-02	0.0
			0.414352D+02	0.451130D-01	0.0
0.936699D+00			0.192694D+00	0.0	
0.253773D+01			0.468544D+00	0.0	
0.746637D+00			0.440608D+00	0.0	
2sp		0.692397D+00	-0.252537D+00	0.143592D+00	
		0.821924D-01	0.109734D+01	0.947803D+00	
2sp		0.322375D-01	0.100000D+01	0.100000D+01	
O		1s	0.883273D+03	0.175506D-01	0.0
			0.133129D+03	0.122829D+00	0.0
	0.299064D+02		0.434884D+00	0.0	
	0.798608D+01		0.560011D+00	0.0	
	2sp	0.165233D+02	-0.113401D+00	0.685453D-01	
		0.385684D+01	0.177286D+00	0.331225D+00	
		0.109273D+01	0.115041D+01	0.734608D+00	
	2sp	0.295585D+00	0.100000D+01	0.100000D+01	

CHAPTER III

RESULTS AND DISCUSSION

The optimized equilibrium geometry and total energy for $[\text{CO}_3]^{2-}$ are found in Table III. For a small ion with such well defined bond character, it would be expected that changing the basis set for the calculation would not have very much effect on the final equilibrium geometry. By comparison of the equilibrium geometries in Table III for $[\text{CO}_3]^{2-}$ at the 3-21G and 4-31G levels, this is found to indeed be the case. The bond angles are identical, and the bond lengths agree to four significant figures. The calculated restricted Hartree-Fock energy is lower for the 4-31G basis set, as is expected; however, these energies have been used in this study for comparison purposes only, to determine which of two or more equilibrium structures calculated has the lowest total energy, and thus which is the most stable, or preferred structure. The Gaussian 82 computations support the knowledge that $[\text{CO}_3]^{2-}$ is a planer ion with D_{3h} symmetry.

TABLE III. Equilibrium geometries for $[\text{CO}_3]^{2-}$ at 3-21G and 4-31G levels. Energies are from restricted Hartree-Fock calculations.



	bond length(angstroms)			bond angle(degrees)	
	3-21G	4-31G		3-21G	4-31G
C-O1	1.3052	1.3047	O1-C-O2	120.0	120.0
C-O2	1.3052	1.3047	O1-C-O3	120.0	120.0
C-O3	1.3052	1.3047	O2-C-O3	120.0	120.0

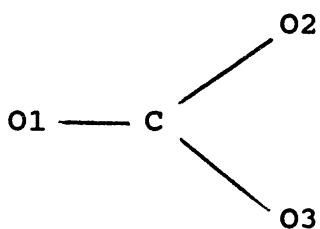
3-21G E(rhf) = -260.737161023 a.u.

4-31G E(rhf) = -261.878479465 a.u.

The total electron densities and net charges for $[\text{CO}_3]^{2-}$ are found in Table IV. The 4-31G basis set provides a more accurate description of the electron densities of each atom in the molecule. The calculations using 4-31G indicate a more polar character of the carbon-oxygen bond length than with 3-21G, and thus the C-O bond length calculated at the 4-31G level should be slightly shorter. This is found to be the case. Frequencies for $[\text{CO}_3]^{2-}$ were calculated using the 3-21G basis set, and they are tabulated in Table V, along with experimental frequencies measured by Nakamoto.²⁶ The Gaussian 82 program correctly predicts the doubly degenerate high frequency stretch and the doubly degenerate in-plane deformation. However, the calculated frequencies are, in general, about ten percent too high. As alkali-metal cations are added and perturb the carbonate anion, the doubly degenerate frequencies will be expected to split. Also, the Raman active but IR forbidden symmetric stretch at 1063 cm^{-1} will be expected to become IR active.

Equilibrium geometries, energies, electron densities, and net charges for $\text{Li}_2[\text{CO}_3]$ and $\text{Na}_2[\text{CO}_3]$ at the 3-21G level may be found in Table VI through IX. During the geometry optimization procedures for these molecules, all atoms were allowed to move unconstrained

TABLE IV. Total electron densities and net charges for $[\text{CO}_3]^{2-}$ at 3-21G and 4-31G levels.



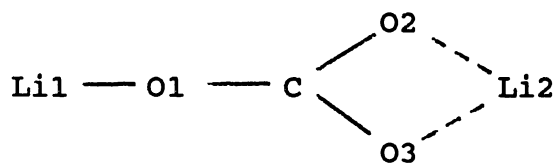
	electron density		net charge	
	3-21G	4-31G	3-21G	4-31G
C	5.084871	5.075078	+0.915129	+0.924922
O1	8.971710	8.974974	-0.971710	-0.974974
O2	8.971710	8.974974	-0.971710	-0.974974
O3	8.971710	8.974974	-0.971710	-0.974974

TABLE V. Calculated and observed frequencies for $[\text{CO}_3]^{2-}$. The frequencies are calculated at the 3-21G level. All frequencies are (cm^{-1}).

observed ^a	calculated	mode	
1415 (doubly degenerate)	1565.3836 1565.3832	E'	stretch
1063 (IR forbidden)	1062.2492	A ₁ '	symmetric stretch
879	970.5360	A ₂ "	symmetric out-of-plane bend
680 (doubly degenerate)	725.1408 725.1406	E'	in-plane deformation

^aTaken from Ref. 26.

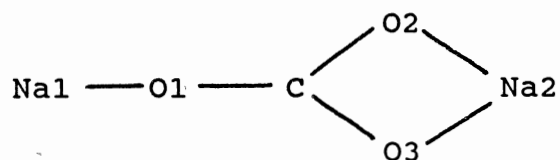
TABLE VI. Equilibrium geometry and restricted Hartree-Fock energy of $\text{Li}_2[\text{CO}_3]$ at 3-21G level.



bond length(angstroms)		bond angle(degrees)	
Li1-O1	1.5914	Li1-O1-C	179.83
O1-C	1.2851	O1-C-O2	121.71
O2-C	1.2958	O1-C-O3	121.71
O3-C	1.2958	C-O2-Li2	84.05
O2-Li2	1.8037	O2-C-O3	116.58
O3-Li2	1.8038		

$$E(\text{rhf}) = -275.971022332 \text{ a.u.}$$

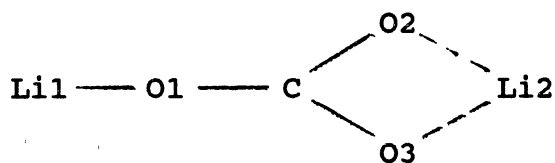
TABLE VII. Equilibrium geometry and restricted Hartree-Fock energy of $\text{Na}_2[\text{CO}_3]$ at 3-21G level.



bond length(angstroms)		bond angle(degrees)	
Na1-O1	1.9145	Na1-O1-C	180.0
O1-C	1.2871	O1-C-O2	120.75
O2-C	1.2968	O1-C-O3	120.76
O3-C	1.2968	C-O2-Na2	88.59
O2-Na2	2.0982	O2-C-O3	118.48
O3-Na2	2.0952		

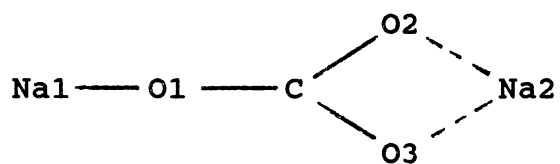
$$E(\text{rhf}) = -582.829424001 \text{ a.u.}$$

TABLE VIII. Total electron densities and net charges for $\text{Li}_2[\text{CO}_3]$ at the 3-21G level.



	electron density	net charge
C	4.828084	+1.171916
Li1	2.324434	+0.675566
Li2	2.459710	+0.540290
O1	8.847582	-0.847582
O2	8.770076	-0.770076
O3	8.770114	-0.770114

TABLE IX. Total electron densities and net charges for $\text{Na}_2[\text{CO}_3]$ at the 3-21G level.



	electron density	net charge
C	4.887456	+1.112544
Na1	10.241778	+0.758222
Na2	10.346053	+0.653947
O1	8.878774	-0.878774
O2	8.822744	-0.822744
O3	8.823196	-0.823196

by any artificial prerequisites. For example, although it is expected that the bond distances for C-O2 and C-O3 are equivalent, they were allowed to change independently of each other, and were not required by the program to be equal. This procedure was followed wherever other expected equivalencies of bond angles and bond distances existed. While this procedure greatly increased the computational time required for convergence to an equilibrium geometry for each molecule (more degrees of freedom), it was necessary to allow for the existence of more than one possible "equilibrium" structure. If more than one "equilibrium" structure were to be found, a comparison of the total energy for each structure would determine which structure was the most stable. Thus, at convergence, the equivalent bond distances and bond angles are slightly different. The C_{2v} symmetry of these ion triplets is obvious, but due to the slightly unequal distances and/or angles, the Gaussian 82 program only recognizes C_s symmetry, and views the molecules as asymmetric tops. This is important only in the fact that in the frequency portion of the program, the task of assigning the vibrational modes to the calculated frequencies becomes more difficult, since the modes assigned by the program are now designated as C_s , and not the expected C_{2v} .

The Li1-O1 bond distance is shorter than the Na1-O1 bond distance, and the Li2-O2 and Li2-O3 equivalent distances are shorter than the Na2-O2 and Na2-O3 distances. As would be expected, the distance increases as the alkali-metal size increases. The O1-C-O2 and O1-C-O3 equivalent bond angles decrease for Na₂[CO₃] as compared to Li₂[CO₃]. Likewise, the O2-C-O3 bond angle is larger for Na₂[CO₃]. Also, the C-O2-Na2 and C-O3-Na2 bond angles are larger than for the comparable bond angles in Li₂[CO₃]. This indicates that as the size of the alkali-metal is increased, the equivalent oxygen atoms move away from the alkali-metal center and away from each other, and move slightly toward the carbon. The total effect is one of less distortion of the [CO₃]²⁻ ion, as is expected.

The most interesting aspect of the equilibrium geometries is that the single unique C-O1 bond is shorter than, and thus is expected to be stronger than, the two equivalent C-O2 and C-O3 bonds. This is in disagreement with the results found by David and Ault¹⁹ and Ogden and Williams,¹⁸ who determined that the single unique C-O bond is weaker than the two equivalent C-O bonds. Unfortunately, there may be no direct comparison of these sets of data, as their experimental results are for potassium and larger alkali-metals,

while the Gaussian 82 basis sets have only been devised for elements through the second row. However, where the lithium atoms were replaced with sodium atoms, the calculations show that the C-O1 distance increased twice as much as the C-O2 and C-O3 distances. This gives rise to the speculation that if sodium were replaced with potassium, the relative strengths of the bonds would be reversed, i.e. both sets of data may be correct. This trend is also supported by the electron densities tabulated in Tables VIII and IX. The electron densities on the oxygens and carbon have all increased for $\text{Na}_2[\text{CO}_3]$. However, the electron density on O1 has increased by a lesser amount than on O2 and O3. If this trend were to continue, there would reach a point where the electron densities on O2 and O3 were greater than on O1, and thus the C-O2 and C-O3 bonds would be termed stronger, not weaker than the C-O1 bond. However, these trends may not follow at all if the observed changes are just due to the reduced cation effect. Clearly, more calculations with a higher basis set need to be done in order to determine whether or not the experimental data is correct.

Frequencies calculated by the Gaussian 82 program for $\text{Li}_2[\text{CO}_3]$ and $\text{Na}_2[\text{CO}_3]$ at the 3-21G level are given in Tables X and XI. Of interest is the extra in-plane

TABLE X. Calculated frequencies and splittings for $\text{Li}_2[\text{CO}_3]$ at 3-21G level. Frequencies are (cm^{-1}). Vibrational mode designations are C_{2v} . Diagrams show the major contributions to the vibrational modes by the various centers, with the length of the arrows indicative of the relative contribution of each center with respect to each other.

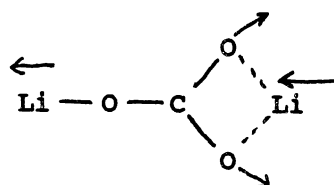
frequency	splitting	mode	motion diagram
1677.1447	177.4	A_1	
1499.7320	----	B_2	
1219.3445	----	A_1	
938.9307	----	A_1	
918.3950	----	B_1	

TABLE X (Continued)

783.6211

A₁

75.7



707.9089

B₂

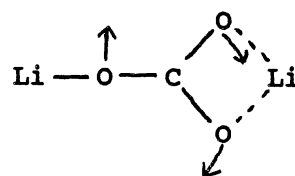


TABLE XI. Calculated frequencies and splittings for $\text{Na}_2[\text{CO}_3]$ at 3-21G level. Frequencies are (cm^{-1}). Vibrational mode designations are C_{2v} . Diagrams show the major contributions to the vibrational modes by the various centers, with the length of the arrows indicative of the relative contribution of each center with respect to each other.

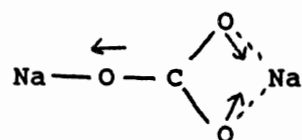
frequency	splitting	mode	motion diagram
1637.2100	138.8	A_1	
1498.4204	----	B_2	
1138.2490	----	A_1	
929.9233	----	B_1	

TABLE XI (Continued)

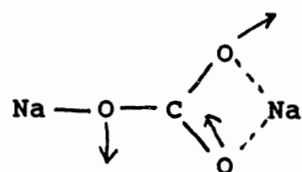
816.7098

 A_1

101.1



715.6227

 B_2 

stretch for $\text{Li}_2[\text{CO}_3]$ at 938.9 cm^{-1} which is not present in $\text{Na}_2[\text{CO}_3]$. The major contributions of this vibration are the Li movement away from the C along the Li1-O1-C-Li2 axis, and the mirrored movements of the O2 and O3 away from each other at right angles to the Li1 movement. This vibrational mode is also present for the $\text{Na}_2[\text{CO}_3]$, but it occurs at 330.1 cm^{-1} , and cannot be measured experimentally. Table XII lists calculated and experimentally measured vibrational frequencies for the series of alkali-metal carbonates. Although the actual calculated frequencies are too high, the calculated splitting magnitudes of the degenerate modes for the lithium and sodium ion triplets are comparable to the experimental splitting magnitudes for the heavier alkali-metals.

The equilibrium geometry, electron densities, net charges, and calculated vibrational frequencies for $\text{Li}_2[\text{CO}_3]$ at the 4-31G level are given in Tables XIII through XV. The 3-21G and 4-31G data are virtually identical with one notable exception. The frequency of the out-of-plane bend calculated at the 4-31G level is higher than the frequency of the in-plane stretch associated with the movement of the Li1/O2/O3 atoms, whereas the reverse is true for the frequencies calculated at the 3-21G level. However, the actual calcu-

TABLE XII. Calculated and observed frequencies for alkali-metal carbonates. All frequencies are (cm^{-1}). $\text{Li}_2[\text{CO}_3]$ is the only ion triplet which has a high frequency vibration (938 cm^{-1}) associated with the movement of one of the alkali-metal cations.

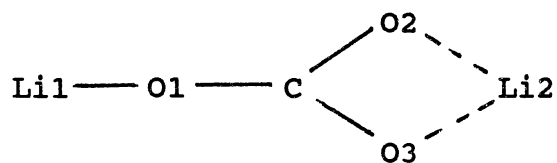
$\text{Li}_2[\text{CO}_3]^a$	$\text{Na}_2[\text{CO}_3]^a$	$\text{K}_2[\text{CO}_3]^b$	$\text{Rb}_2[\text{CO}_3]^b$	$\text{Cs}_2[\text{CO}_3]^b$	$\text{Tl}_2[\text{CO}_3]^c$
1677	1637	1471.6	1467.1	1461.5	1506
1500	1498	1317.4	1320.9	1318.9	1311
1219	1138	1010.1	1016.2	1018.0	1038
938	---	---	---	---	---
918	930	869.8	870.6	870.8	845
783	817	696.7	690.8	684.7	720

^aCalculated at 3-21G level

^bTaken from Ref. 18.

^cTaken from Ref. 19.

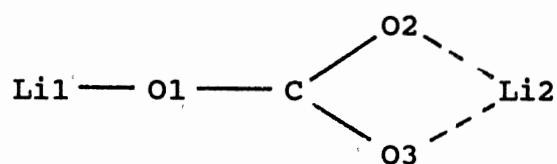
TABLE XIII. Equilibrium geometry and restricted Hartree-Fock energy of $\text{Li}_2[\text{CO}_3]$ at 4-31G level.



bond length(angstroms)		bond angle(degrees)	
Li1-O1	1.6233	Li1-O1-C	179.98
O1-C	1.2820	O1-C-O2	121.72
O2-C	1.2932	O1-C-O3	121.72
O3-C	1.2931	C-O2-Li2	85.09
O2-Li2	1.8432	O2-C-O3	116.56
O3-Li2	1.8436		

$E(\text{rhf}) = -277.124762475 \text{ a.u.}$

TABLE XIV. Total electron densities and net charges for $\text{Li}_2[\text{CO}_3]$ at the 4-31G level.



	electron density	net charge
C	4.881546	+1.118454
Li1	2.219054	+0.780946
Li2	2.313451	+0.686549
O1	8.930540	-0.930540
O2	8.827785	-0.827785
O3	8.827623	-0.827623

TABLE XV. Calculated frequencies and splittings for $\text{Li}_2[\text{CO}_3]$ at 4-31G level. Frequencies are (cm^{-1}). Vibrational mode designations are C_{2v} . Diagrams show the major contributions to the vibrational modes by the various centers, with the length of the arrows indicative of the relative contribution of each center with respect to each other.

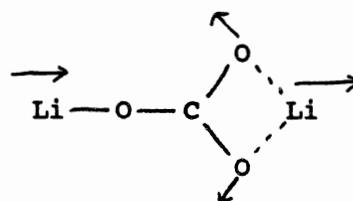
frequency	splitting	mode	motion diagram
1685.9953		A_1	
	162.5		
1523.4740	----	B_2	
1203.7692	----	A_1	
918.0209	----	B_1	
907.4165	----	A_1	

TABLE XV (Continued)

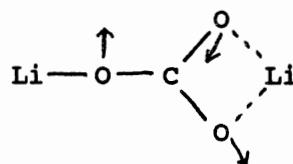
743.2826

 A_1

39.3



704.0475

 B_2 

lated frequencies are too high, although the splitting of the degenerate modes has decreased somewhat. The 4-31G basis set calculations otherwise support the trends discussed for the 3-21G basis set for $\text{Li}_2[\text{CO}_3]$.

Of paramount interest for the alkali-metal carbonates is the question of whether there exists a stable equilibrium structure where both of the metal centers are bidentate to the carbonate anion. The data of Ogden and Williams¹⁸ do not preclude the possibility of such a structure. Therefore, the Gaussian 82 program was used to conduct a search for a different stable equilibrium geometry in the cases of both $\text{Li}_2[\text{CO}_3]$ and $\text{Na}_2[\text{CO}_3]$. This was accomplished by inputting a "best guess" doubly bidentate initial starting structure. The Gaussian 82 options were set for STEEP and OPTCYC=60, and then the various atoms were allowed to move without predetermined constraints along the direction of steepest descent. In each case, the ion triplet eventually moved and settled into the equilibrium structure reported here, i.e. an anion with a bidentate metal cation and a monodentate metal cation. No saddle points were found, and thus it is concluded that for $\text{Li}_2[\text{CO}_3]$ and $\text{Na}_2[\text{CO}_3]$ there is no "stable" doubly bidentate structure.

CHAPTER IV

CONCLUSIONS

Equilibrium geometries, electron distributions, and vibrational frequencies have been computed for $[\text{CO}_3]^{2-}$, $\text{Li}_2[\text{CO}_3]$, and $\text{Na}_2[\text{CO}_3]$ using the Gaussian 82 system of programs at the 3-21G and 4-31G levels. The calculated bond lengths, and thus bond strengths of the O1-C, O2-C, and O3-C bonds were found to be reversed from reported experimentally measured bond strengths of these same bonds for the heavier alkali-metal carbonates. Trends indeed suggest that the relative strengths of these bonds may switch between $\text{Na}_2[\text{CO}_3]$ and $\text{K}_2[\text{CO}_3]$. Calculated vibrational frequencies were computed for $[\text{CO}_3]^{2-}$, $\text{Li}_2[\text{CO}_3]$, and $\text{Na}_2[\text{CO}_3]$ at the 3-21G level. The calculated frequencies were found to be consistently too high; however, the prediction of degenerate vibrational modes for $[\text{CO}_3]^{2-}$, and the predicted values of the degenerate mode splittings for the distorted anions are in fair agreement with literature values for the heavier alkali-metal carbonates. The equilibrium geometries for $\text{Li}_2[\text{CO}_3]$ and $\text{Na}_2[\text{CO}_3]$ are

found to both have one monodentate and one bidentate metal center. No doubly bidentate equilibrium structure was found. Higher basis set calculations for the $\text{Li}_2[\text{CO}_3]$ ion triplet were essentially the same as the lower basis set calculations, and no fundamental differences were found in the calculated equilibrium geometries or electron densities.

BIBLIOGRAPHY

- ¹D.E. Irish and M.H. Brooker in Advances in Infrared and Raman Spectroscopy Vol. 2, Chap. 6, (R.J.H. Clark and R.E. Hester, eds.), Heyden, London, 1976.
- ²D.J. Gardiner in Advances in Infrared and Raman Spectroscopy Vol. 3, Chap. 5, (R.J.H. Clark and R.E. Hester, eds.), Heyden, London, 1978.
- ³J.P. Devlin in Advances in Infrared and Raman Spectroscopy Vol. 2, Chap. 5, (R.J.H. Clark and R.E. Hester, eds.), Heyden, London, 1976.
- ⁴J.K. Wilmhurst, J. Chem. Phys. 36, 2415 (1962).
- ⁵B.G. Oliver and G.J. Janz, J. Phys. Chem. 75, 2948 (1971).
- ⁶R. Giebelmann, Pharmazie 41, 748 (1986).
- ⁷D.J. Gardiner, R.B. Girling, and R.E. Hester, J. Mol. Struct. 13, 105 (1972).
- ⁸L.L. Simmons, L.F. Lowden, and T.C. Ehlert, J. Phys. Chem. 81, 706 (1977).
- ⁹N. Smyrl and J.P. Devlin, J. Chem. Phys. 60, 2540 (1974).
- ¹⁰L. Bencivenni, K.A. Gingerich, and R. Teghil, J. Chem. Phys. 81, 3415 (1984).
- ¹¹D.M. Hercules, Springer Proc. Phys. 9, 147 (1986).
- ¹²R.D. Amos, CADPAC, SERC Daresbury Lab. Publ. CCP1/84/4, 1984.
- ¹³J.S. Francisco and I.H. Williams, Chem. Phys. 114, 339 (1987).
- ¹⁴J.S. Francisco and I.H. Williams, Chem. Phys. 120, 389 (1988).

- ¹⁵W.J. Hehre, L. Radom, P.R. Schleyer, and J.A. Pople, Ab Initio Molecular Orbital Theory, John Wiley and Sons, New York, 1986.
- ¹⁶J.C. Halle and K.H. Stern, J. Phys. Chem. **84**, 1699 (1980).
- ¹⁷J.P. Devlin, Vib. Spectra Struct. **16**, 73 (1987).
- ¹⁸J.S. Ogden and S.J. Williams, J. Chem. Soc., Dalton Trans., 456 (1981).
- ¹⁹S.J. David and B.S. Ault, J. Phys. Chem. **86**, 4618 (1982).
- ²⁰W.J. Hehre, R.F. Stewart, and J.A. Pople, J. Chem. Phys. **51**, 2657 (1969).
- ²¹M.M. Franci, W.J. Pietro, W.J. Hehre, J.S. Binkley, M.S. Gordon, D.J. DeFrees, and J.A. Pople, J. Chem. Phys. **77**, 3654 (1982).
- ²²R. Ditchfield, W.J. Hehre, and J.A. Pople, J. Chem. Phys. **54**, 724 (1971).
- ²³J.S. Binkley, M.J. Frisch, D.J. DeFrees, K. Raghavachari, R.A. Whiteside, H.B. Schlegel, and J.A. Pople, Gaussian 82 (Rev. H 28-Nov. 1983), Carnegie-Mellon University, Pittsburgh, PA 15213.
- ²⁴A.D. McLean and G.S. Chandler, J. Chem. Phys. **72**, 5639 (1980).
- ²⁵A. Szabo and N.S. Ostlund, Modern Quantum Chemistry: Introduction to Advanced Electronic Structure Theory, MacMillian Publishing Company, New York, New York, 1983.
- ²⁶K. Nakamoto, Infrared and Raman Spectra of Inorganic and Coordination Compounds, 3rd ed., Wiley Interscience, New York, 1978.

CHAPTER I

INTRODUCTION

van der Waals molecules are weakly bound complexes of atoms or molecules held together, not by chemical bonds, but by dispersive molecular forces. Traditional interest in van der Waals molecules has been due to their importance in nucleation phenomena and their role in determining the bulk properties of solids and liquids.¹ Consequently, much effort has been devoted to the determination of properties of van der Waals bonding.² In recent years, however, a great deal of attention has been devoted to understanding the chemical dynamics of such molecules. Molecular beam studies have provided direct evidence of the presence of van der Waals molecules in chemical reactions. Crossed molecular beam studies by King, Dixon, and Herschbach³ of the reaction $(\text{Cl}_2)_2 + \text{Br}_2 \rightarrow \text{Cl}_2 + 2 \text{BrCl}$ clearly illustrate how van der Waals molecules can play a role in exchange reactions.

The simplest bond exchange process is a rare gas atom--rare gas dimer collision. Rare gas dimers are

weakly bound; however, such dimers have well defined rotational and vibrational states which have been experimentally characterized. The kinetic behavior of such monomer-dimer collisions must be completely understood in order to correctly describe the initial stages of condensation, and as a basis for the study of more complex systems involving larger clusters. We have reported quasiclassical trajectory studies of rare gas atom-dimer collisional processes for the reactions of $\text{Ar} + \text{Ar}_2$, $\text{Ar} + \text{Ne}_2$, and $\text{Ar} + \text{ArKr}$.⁴ The distribution of metastable Ar_2 lifetimes was computed using WKB statistical state counting methods. The results show that a significant fraction of the metastable dimers have lifetimes such that they may reach the detector in crossed molecular beam experiments. Further studies of the exchange and dissociation mechanisms for the reactions of $\text{Kr} + \text{NeAr}$, $\text{Kr} + \text{Ar}_2$, and $\text{Xe} + \text{Ar}_2$ have been reported.⁵ The results indicate that mechanistic, as well as statistical, factors are important in the reaction dynamics. Light-atom abstraction was found to occur by a stripping mechanism, whereas abstraction of the heavier atom involves complex formation and rebound scattering. The mechanisms seem to be somewhat energy dependent for some systems, with the heavy-atom abstraction occurring preferentially at higher energies.

The results are, in general, in accord with the molecular beam studies reported by Worsnop, Buelow, and Herschbach⁶ for the $\text{Xe} + \text{Ar}_2$ reaction. Most recently, Ar_2 depletion mechanisms in free-jet expansions of seeded Ar beams have been investigated both experimentally^{7(a)} and theoretically.^{7(b)}

In the present study, quasiclassical trajectory calculations have been used to examine the importance of tunneling for several atom-dimer exchange reactions that include $\text{Ar} + \text{Ar}_2$, $\text{Xe} + \text{Ar}_2$, $\text{Kr} + \text{Ne}_2$, $\text{Kr} + \text{Xe}_2$, and $\text{Kr} + \text{NeAr}$. Statistical counting methods similar to those previously employed⁴ to obtain metastable lifetime distribution for the $\text{Ar} + \text{Ar}_2$ reaction have been used to compute lifetime distributions for several additional three-body reactions. The effect of tunneling upon the exchange and dissociation cross sections and upon the angular and product-velocity distributions have been examined. The possibility of direct detection of such tunneling by variation of the reaction site-detector distance in a crossed molecular beam study of these reactions has been investigated.

CHAPTER II

COMPUTATIONAL PROCEDURE

The potential-energy surfaces were represented by the sum of three Morse potentials. The values of the potential parameters are given in Table I (Refs. 9-15). Plots of the Ne_2 and Xe_2 potentials are shown in Fig. 1 for comparison. The details of the rotational barrier were computed as before,⁴ and the product molecules were counted as stable, metastable, or dissociative, if their final energies were less than D_e , greater than D_e but less than the rotational barrier, or greater than the rotational barrier, respectively. Plots of the potential for NeKr as a function of rotational state are shown in Fig. 2. As the rotational state increases, the barrier height increases, and the potential minimum increases, with a resulting net decrease in the potential difference between the two. The location of the minimum shifts to a larger r , whereas the location of the barrier minimum shifts to smaller r . The net result is a smaller difference between the two. At some large rotational state J_{max} , the potential be-

TABLE I. Pairwise Morse potential parameters.

	D_e (eV)	(a.u.)	(a.u.)
Ne-Ne ^a	0.0036864	1.07535	5.87716
Ne-Ar ^a	0.006201	1.01822	6.48189
Ne-Kr ^a	0.006418	1.03684	6.76535
Ar-Ar ^b	0.01223	0.9234	7.200
Ar-Kr ^c	0.01443	0.9001	7.3323
Ar-Xe ^d	0.016148	1.000	7.6724
Kr-Xe ^e	0.01990	0.8100	7.920
Xe-Xe ^f	0.0237813	0.78189	8.300

^aTaken from Ref. 9.^bTaken from Ref. 10.^cTaken from Ref. 11.^dTaken from Ref. 12.^eTaken from Ref. 13.^fTaken from analysis of
Refs. 14 and 15.

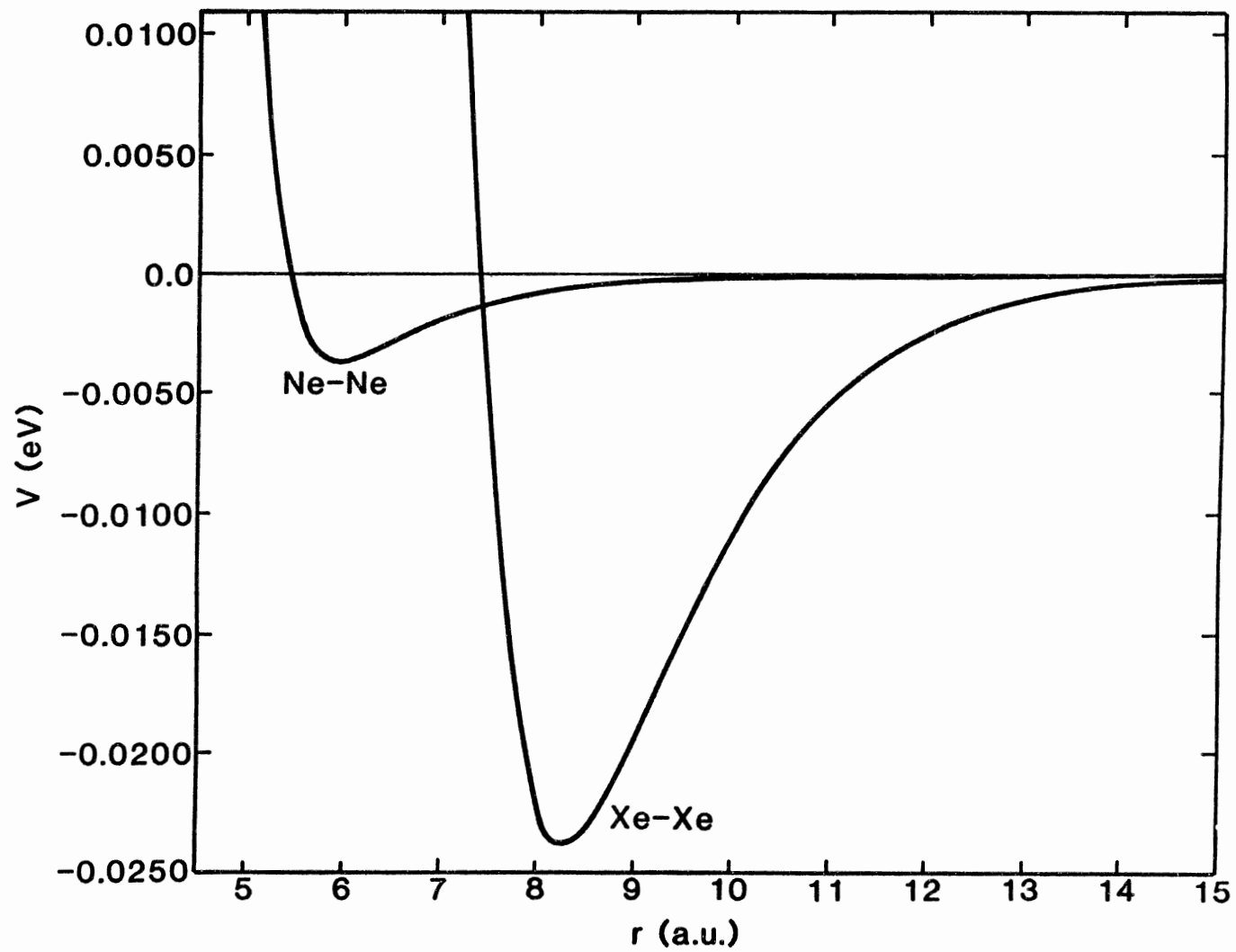


Fig. 1. Plots of the Ne-Ne and Xe-Xe potentials. The Morse parameters are given in Table I.

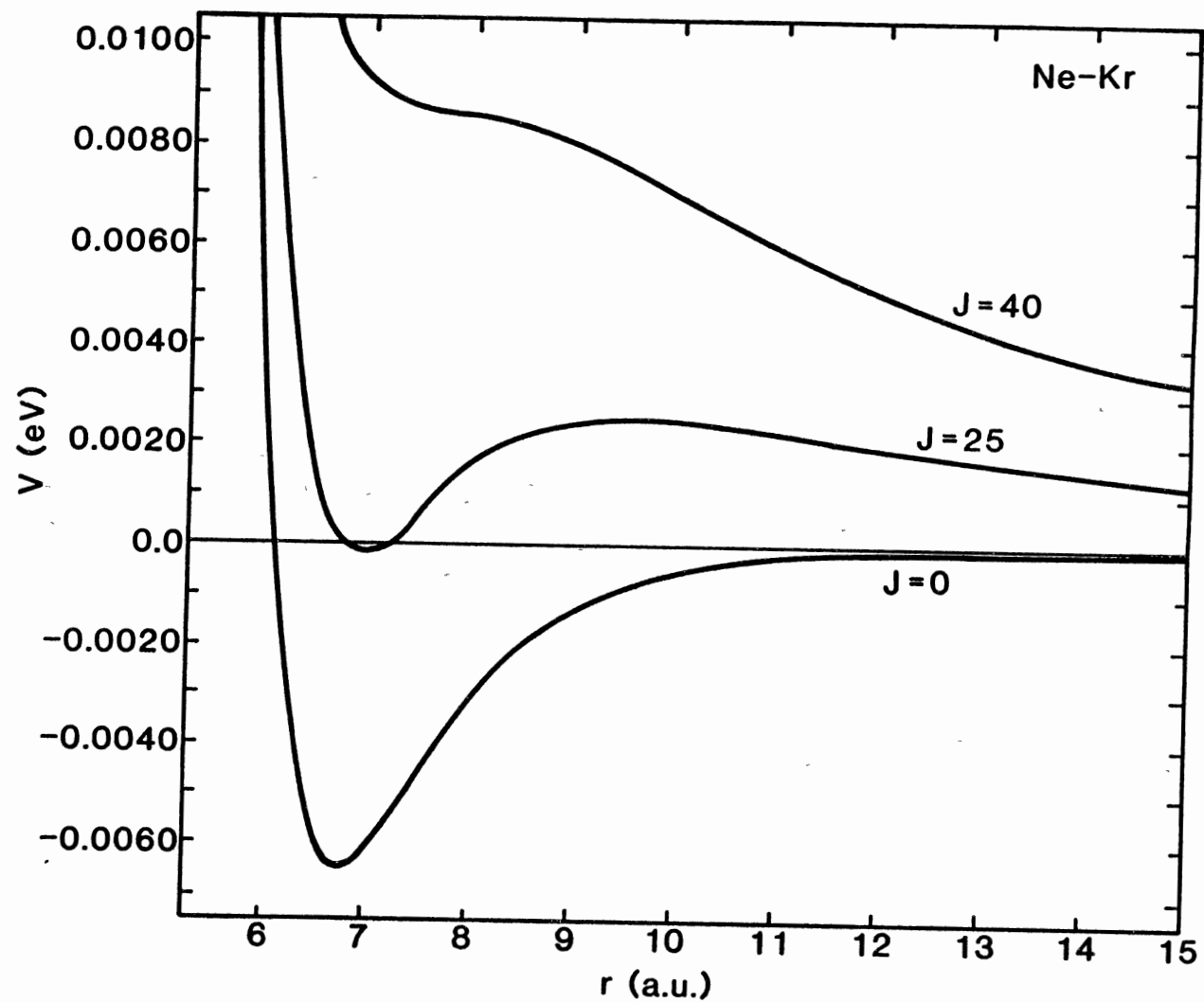


Fig. 2. Plots of the Ne-Kr potential for rotational states $J = 0$, $J = 25$, and $J = 40$.

comes strictly repulsive. This type of behavior is illustrated by the case of NeKr by the effective potential for $J=40$. All molecules having rotational angular momentum quantum numbers greater than J_{\max} are counted as dissociative. The maximum rotational state is a function of the atomic masses, and is thus computed for each type of product diatom.

If a product molecule was determined to be metastable, its lifetime was computed using a WKB procedure.⁴ Using this computed lifetime and the translational velocity of the product molecule, the distance the molecule traveled before dissociation occurred was computed. This distance was compared to the reaction site-detector distance in a typical molecular beam experiment. If a metastable dimer had a lifetime such that it dissociated before reaching the "detector", it was not considered to be a reaction product molecule, and thus was not included in the cross section, angular distribution, or product-velocity distribution for product dimers.

The usual Monte Carlo quasiclassical procedures were employed.⁸ Calculations were performed as a function of the relative translational energy E_{rel} . The initial E_{rel} was chosen from a Boltzmann distribution, or in some cases was fixed as in a velocity-selected

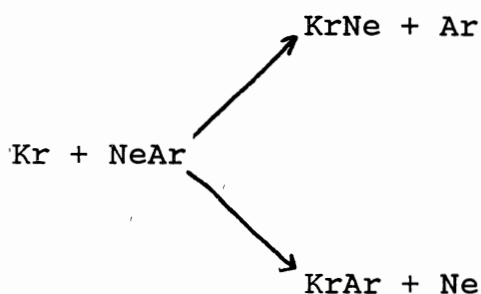
crossed molecular beam experiment. The initial vibrational and rotational states were chosen to be the ground states. The impact parameter was averaged over the range $0 \leq b \leq 16.0$ a.u. Batches of 5000 to 30 000 trajectories were computed. The trajectories were integrated using the fourth-order Runge-Kutta-Gill procedure with 1.616×10^{-14} s stepsize.

The lifetime distributions were also computed by WKB and statistical state counting procedures for comparison with the trajectory results. The bound vibrational-rotational states were computed by the WKB method, and these states were given statistical weights as previously reported.⁴

CHAPTER III

RESULTS AND DISCUSSION

Cross sections for the rare gas exchange reactions were computed as a function of initial relative translational energy E_{rel} . For the reactions



the cross sections for stable and metastable product molecules over the collisional energy range 0.01 to 0.10 eV are shown in Fig. 2 of Ref. 5. In all of the reactions investigated, metastable molecules comprise a significant portion of the final products. It is expected that the role of these metastable dimers will be most pronounced in the energy ranges where they are the major products. Thus, the energy regions of interest for the reaction $\text{Kr} + \text{NeAr}$ were chosen to be 0.010 and

0.025 eV, where the metastable dimers comprise 50% to 60% of the total product. Similar considerations suggest that the relative translational energies of interest for the reactions $\text{Kr} + \text{Xe}_2$ and $\text{Kr} + \text{Ne}_2$ are 0.045 and 0.010 eV, respectively. For the purposes of comparison with previous experimental and theoretical studies,^{5,6} energies of 0.030 and 0.040 eV were chosen for the $\text{Xe} + \text{Ar}_2$ reaction study. The predominant products for the $\text{Kr} + \text{NeAr}$ reaction are dependent upon the collisional energy and the mechanism which describes their formation. The $\text{Kr} + \text{NeAr} \rightarrow \text{KrNe} + \text{Ar}$ reaction occurs primarily by a stripping mechanism, whereby the incoming Kr atom abstracts the Ne atom at large impact parameters. The $\text{Kr} + \text{NeAr} \rightarrow \text{KrAr} + \text{Ne}$ reaction occurs through a more complex, three-body mechanism.⁵

Lifetime distributions for metastables were computed for all five reactions using the WKB tunneling probability. Two lifetime distributions for the $\text{Ar} + \text{Ar}_2 \rightarrow \text{Ar}_2^* + \text{Ar}$ reaction at $E_{\text{rel}} = 0.01735$ eV have been plotted in Fig. 3. The upper graph was computed by giving statistical weights $N(\nu, J')$, to the rotational J states,⁴ where

$$N(\nu, J') = (2J' + 1) \rho(E_{\gamma} - E_{\nu}),$$

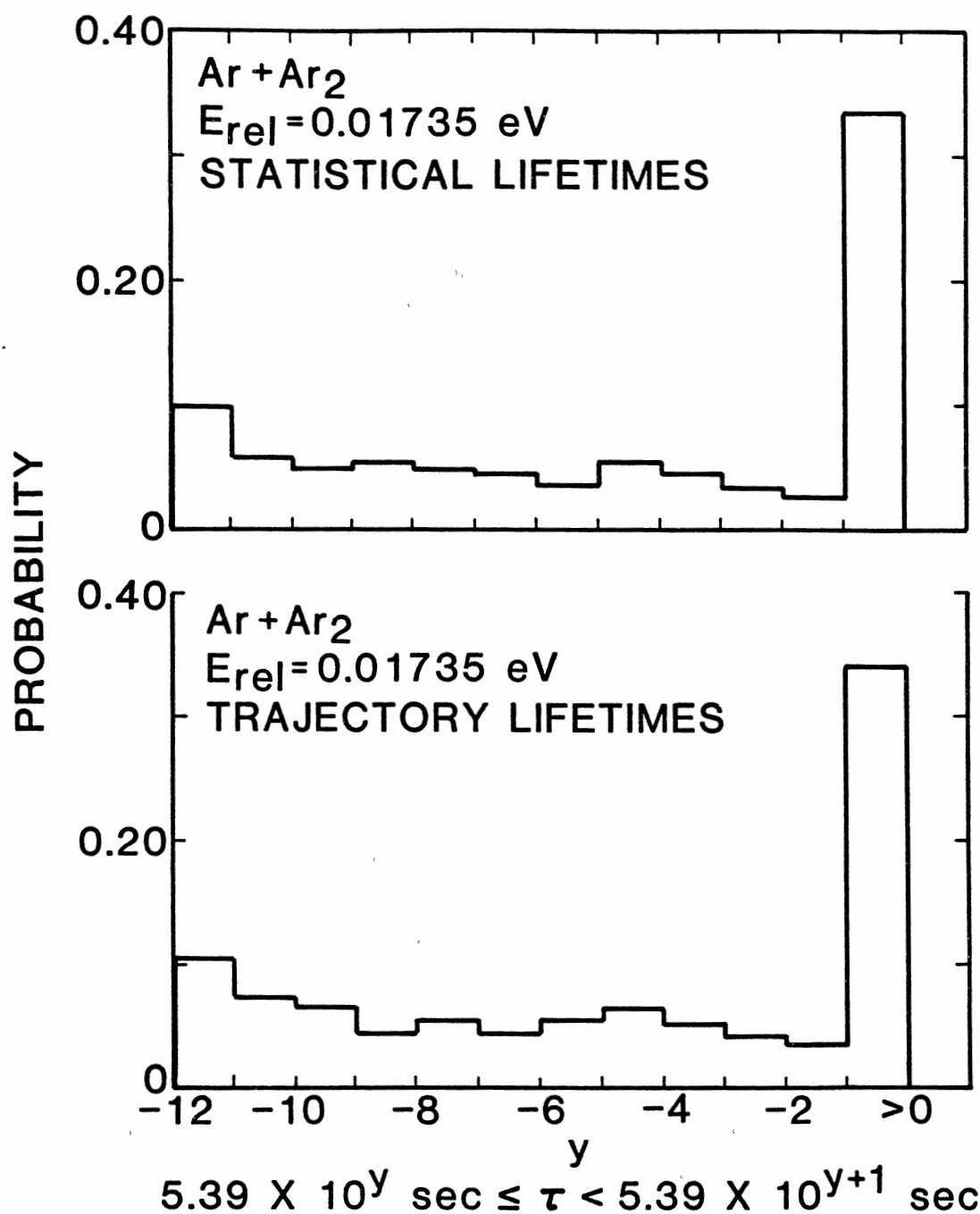


Fig. 3. Distributions of lifetimes for Ar₂^{*} formed by exchange in Ar + Ar₂ collisions at E_{rel} = 0.01735 eV. The upper graph is computed from WKB tunneling probabilities; the lower graph is computed from a batch of 30 000 trajectories. Each histogram block gives the total integrated probability of observing Ar₂^{*} lifetimes in the range $5.39 \times 10^y \text{ s} \leq \tau < 5.39 \times 10^{y+1} \text{ s}$. The histogram block at the far right gives the total integrated probability for observing $5.39 \times 10^{-1} \text{ s}$.

in which E_{γ} is the total energy of the product molecule, and $\rho(E_{\gamma} - E_{\nu})$ is the density of the translational states at $E_{\text{trans}} = E_{\gamma} - E_{\nu}$. E_{ν} represents the vibrational energy of the product molecule. The lower graph was computed from a batch of 30 000 trajectories. There is no significant difference between the two lifetime distributions. About 45% of the metastable dimers dissociate with lifetimes shorter than 10^{-5} s. In a corresponding molecular beam experiment, these dimers would not reach a detector placed approximately 10 cm from the crossed beam reaction site.

Lifetime distributions for the Kr + NeAr system are shown in Figs. 4 and 5 for collisional energies of 0.010 and 0.025 eV. The results were obtained from a batch of 15 000 trajectories at each energy. In Fig. 4, the upper graph is for KrNe product formation at 0.010 eV, while the lower graph is for the same KrNe product at 0.025 eV. Both distributions exhibit the same general features, where molecules with the shortest lifetimes are most probable, and those with longer lifetimes are less probable. The histogram blocks corresponding to the longest lifetimes also include all dimers with lifetimes greater than 5.39 s; thus, the graphs indicate a smooth, gradual decrease in

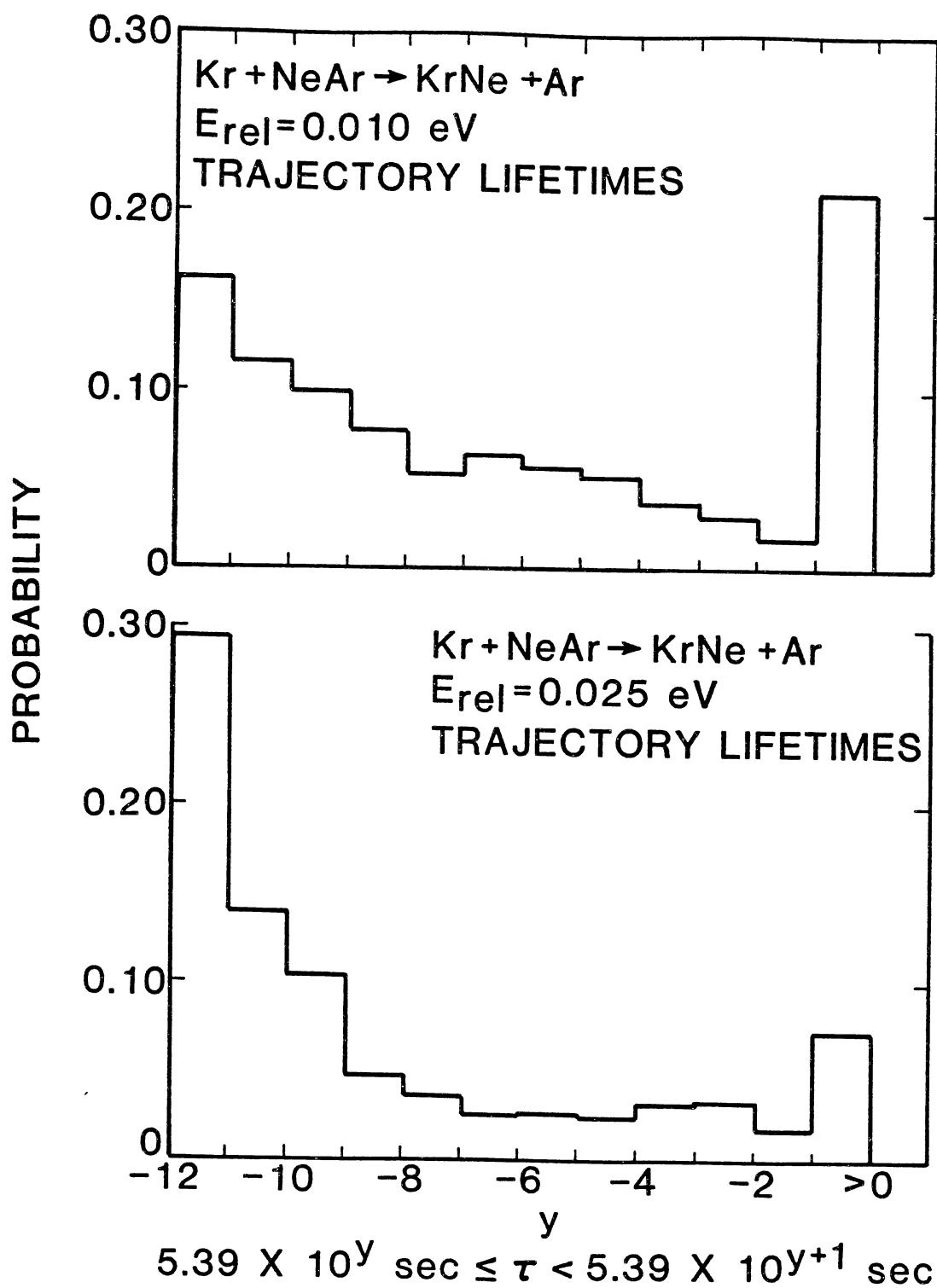


Fig. 4. Distributions of trajectory lifetimes for KrNe formed by exchange in Kr + ArNe collisions at relative collisional energies of 0.010 and 0.025 eV. The histogram blocks represent the same as in Fig. 3.

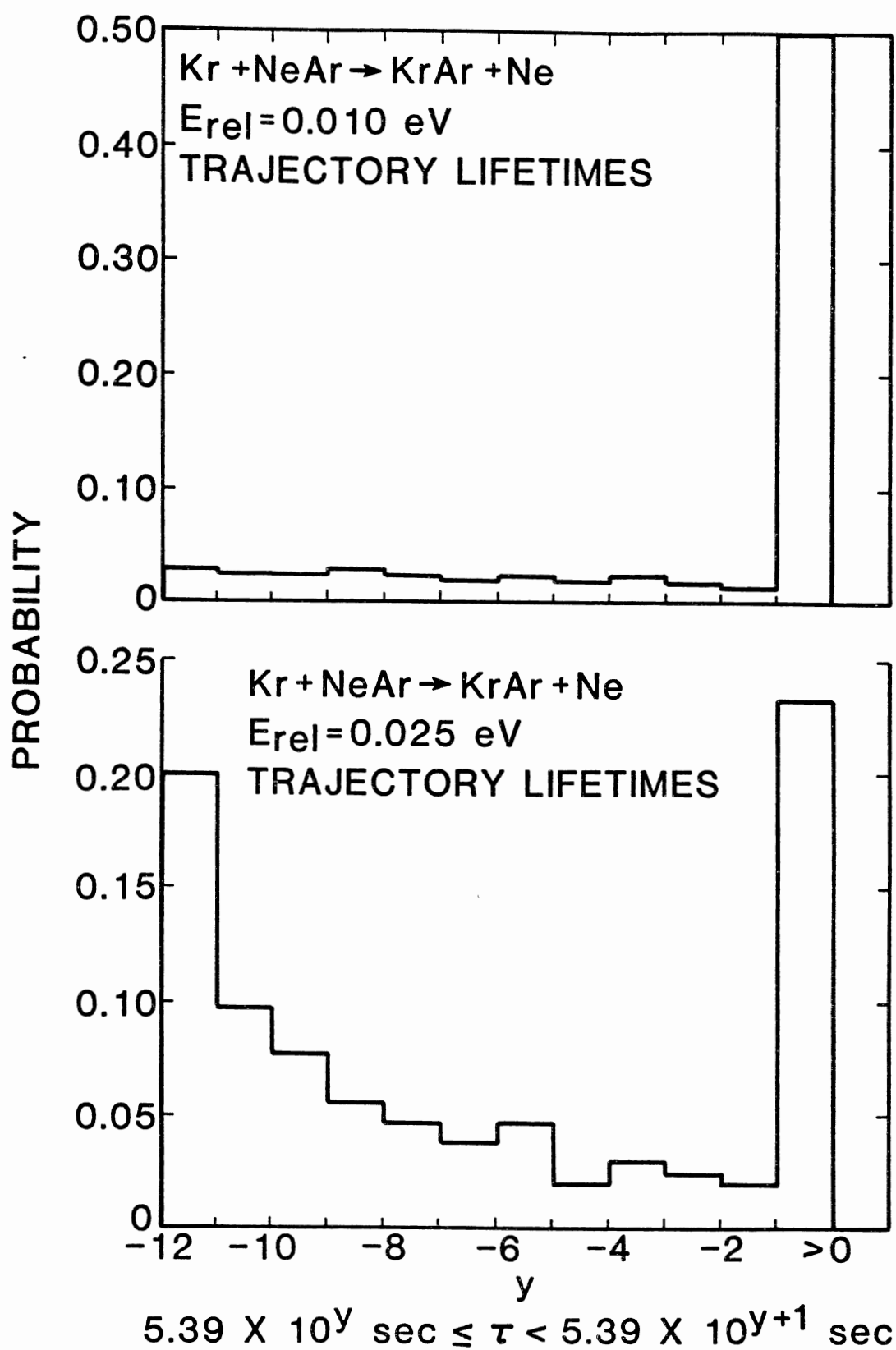


Fig. 5. Same as Fig. 4 except for KrAr exchange product.

probability as the lifetimes increase. However, the short-lived KrNe product is more probable at the higher collisional energy, and there is a corresponding decrease in the probability of long-lived product. Figure 5 shows the lifetime distributions for the KrAr product at the same energies. At 0.01 eV, the shortest-lived product does not predominate, but otherwise the general features are the same as for the KrNe product lifetime distributions. The statistical lifetime distributions for both products at 0.025 eV are shown in Fig. 6. As with the trajectory results, there is a general decrease in probability with increase in lifetime. The agreement between statistical and trajectory results at 0.025 eV suggests that the Kr + NeAr system behaves statistically at high collisional energies.

The lifetime distributions for the Kr + Xe₂ system at 0.045 eV are shown in Fig. 7. The upper graph is for a statistical calculation, and the lower graph is the result of 15 000 trajectories. Both distributions show a relatively constant probability for all lifetimes, and both show that the longer-lived KrXe product predominates. The lifetime distributions for the Kr + Ne₂ system have been plotted in Fig. 8. The lower graph, obtained from 15 000 trajectories, ex-

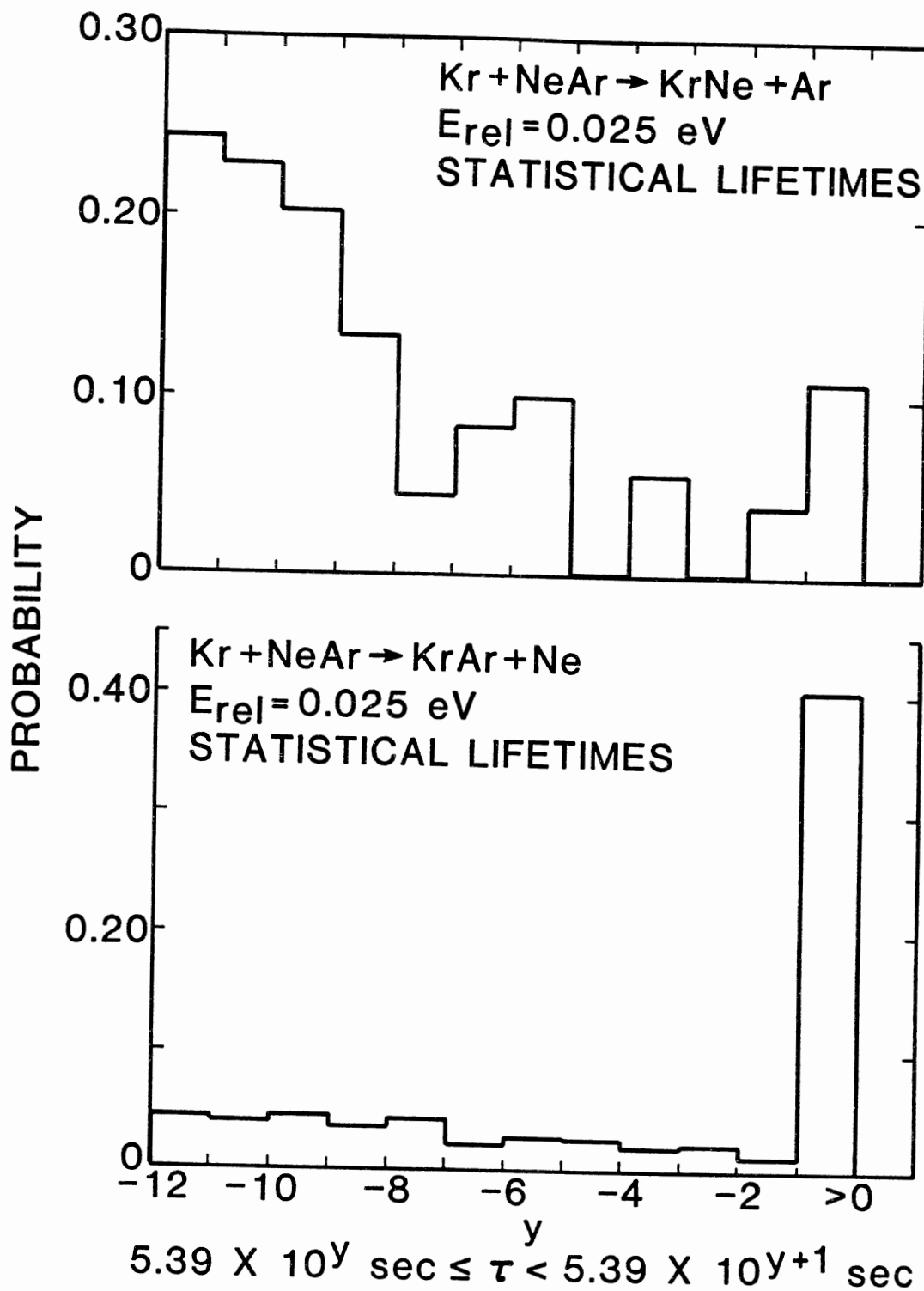


Fig. 6. Distributions of WKB lifetimes for the Kr + NeAr system at $E_{\text{rel}} = 0.025 \text{ eV}$. The upper graph is for the KrNe exchange product; the lower graph is for the ArKr exchange product. The histogram blocks represent the same as in Fig. 3.

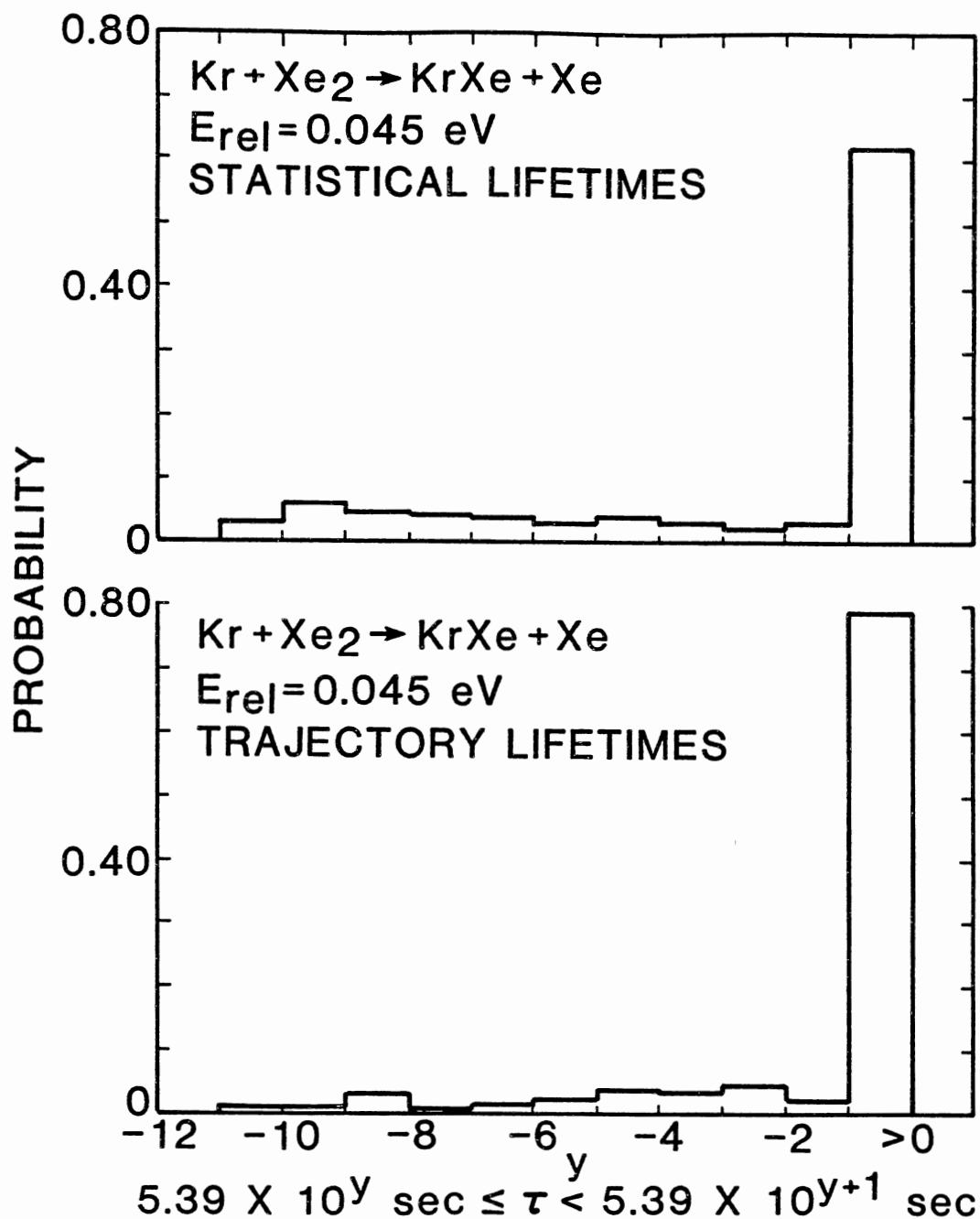


Fig. 7. Distributions of lifetimes for KrXe formed by exchange in $\text{Kr} + \text{Xe}_2$ collisions at $E_{\text{rel}} = 0.045 \text{ eV}$. The upper graph is computed from WKB tunneling probabilities; the lower graph is computed from a batch of 15 000 trajectories. The histogram blocks represent the same as in Fig. 3.

hibits the same behavior as its statistical counterpart at a collisional energy of 0.01 eV. There is again a gradual decrease in probability as the molecule lifetime increases. The lifetime distributions at 0.030 and 0.040 eV for the Xe + Ar₂ system are shown in Fig. 9. These data are the results of 15 000 trajectories. At the higher collisional energy there is a slight increase in shorter lifetime probabilities, but the longest lifetimes are most probable at both energies.

The center-of-mass angular scattering distributions are plotted in Figs. 10-13 for the Kr + NeAr, Kr + Xe₂, Xe + Ar₂, and Kr + Ne₂ reactions. The scattering angle is that angle at which the product molecule is scattered relative to the direction of the initial relative velocity vector. The upper solid lines represent the classical intensities, where the tunneling and subsequent dissociation of the metastable products have been ignored. The lower dotted lines represent the intensities obtained when the tunneling and dissociation of metastables have been taken into account. This is done by direct computation of transit time of the products from the reaction center to a detector 10 cm distant using the laboratory velocity of the reaction products obtained from the trajectory

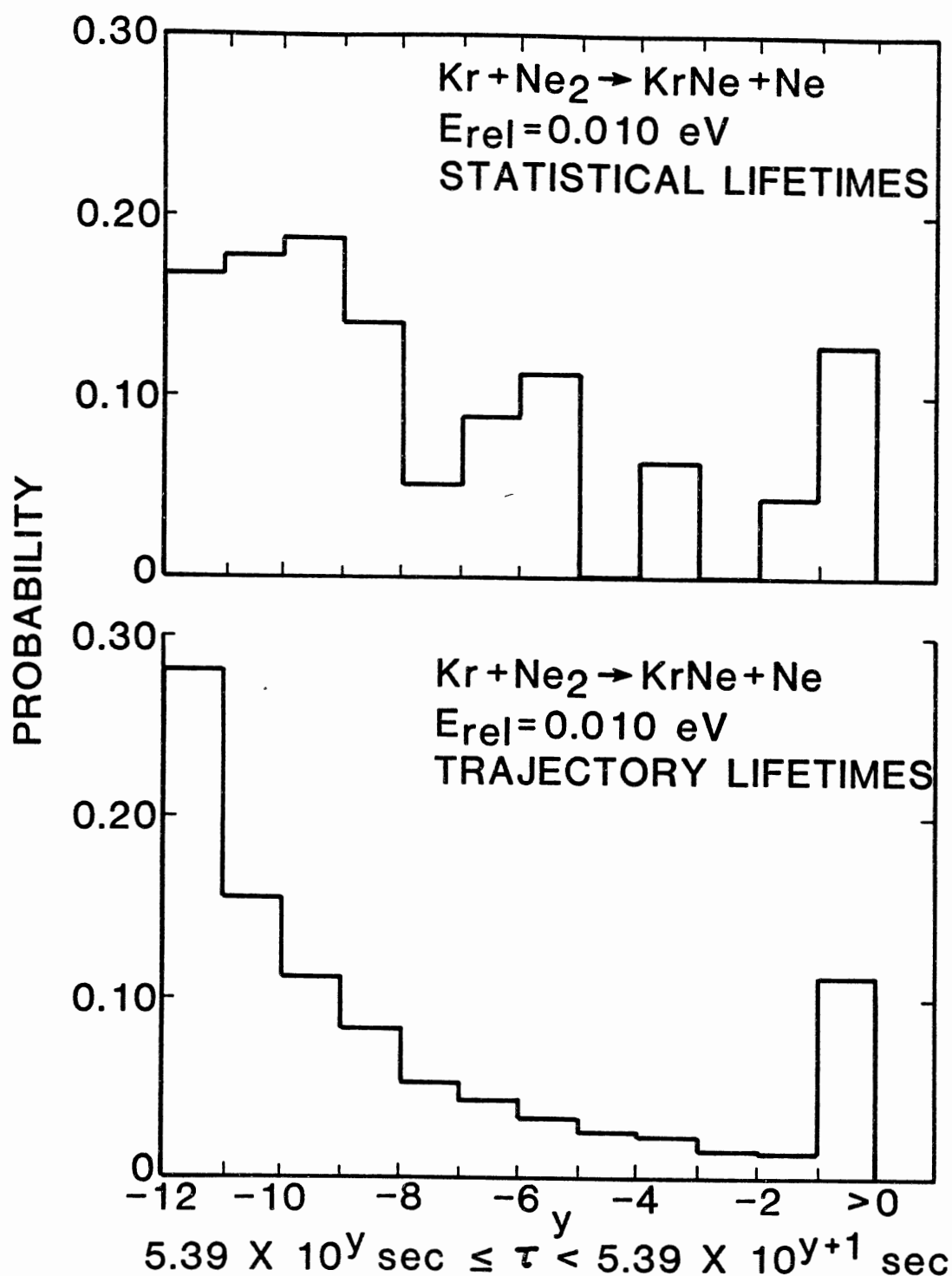


Fig. 8. Distributions of lifetimes for KrNe formed by exchange in $\text{Kr} + \text{Ne}_2$ collisions at $E_{\text{rel}} = 0.010 \text{ eV}$. The upper graph is computed from WKB tunneling probabilities; the lower graph is computed from a batch of 15 000 trajectories. The histogram blocks represent the same as in Fig. 3.

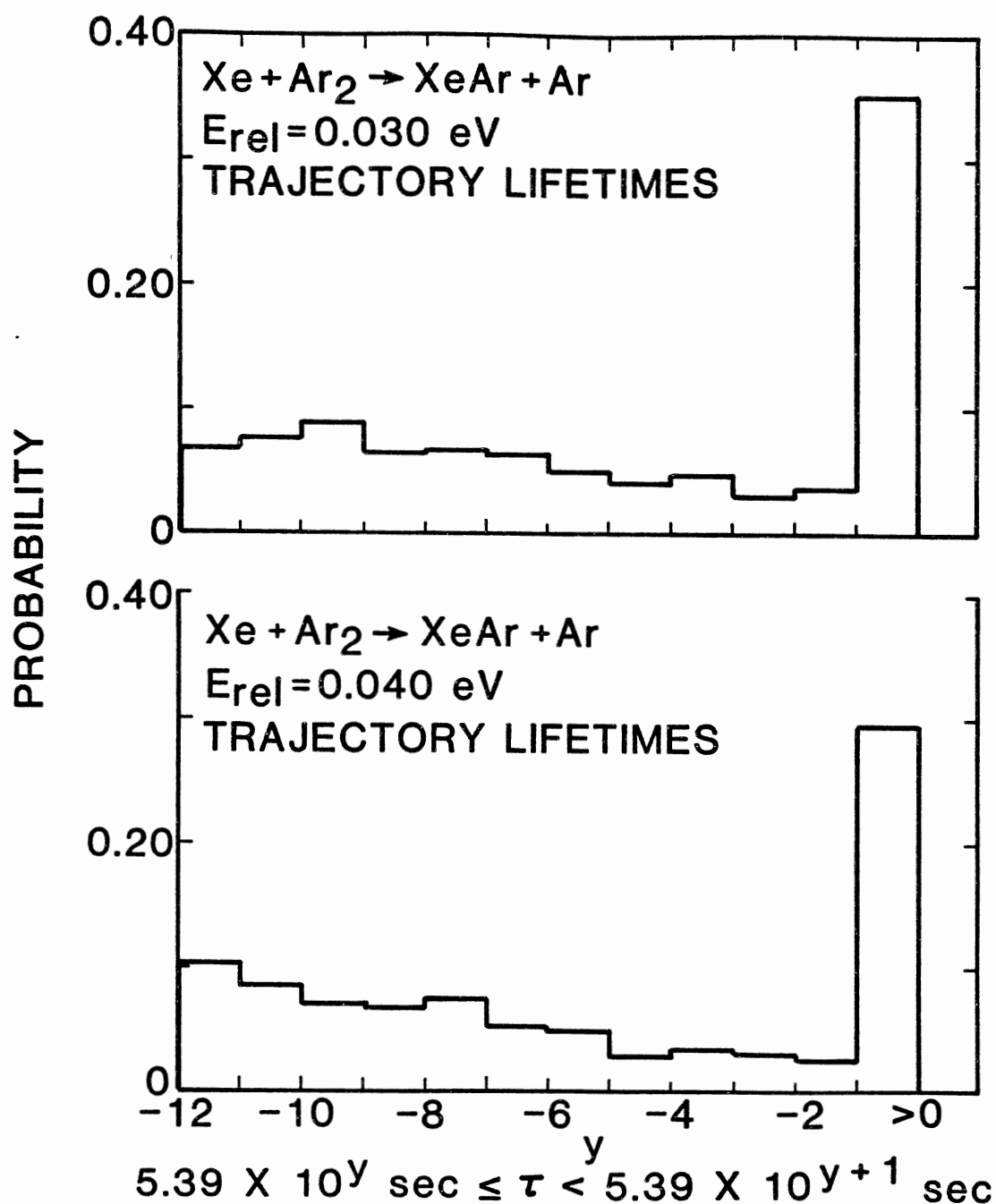


Fig. 9. Distributions of trajectory lifetimes for XeAr formed by exchange in Xe + Ar₂ collisions at relative collisional energies of 0.030 and 0.040 eV. The histogram blocks represent the same as in Fig. 3.

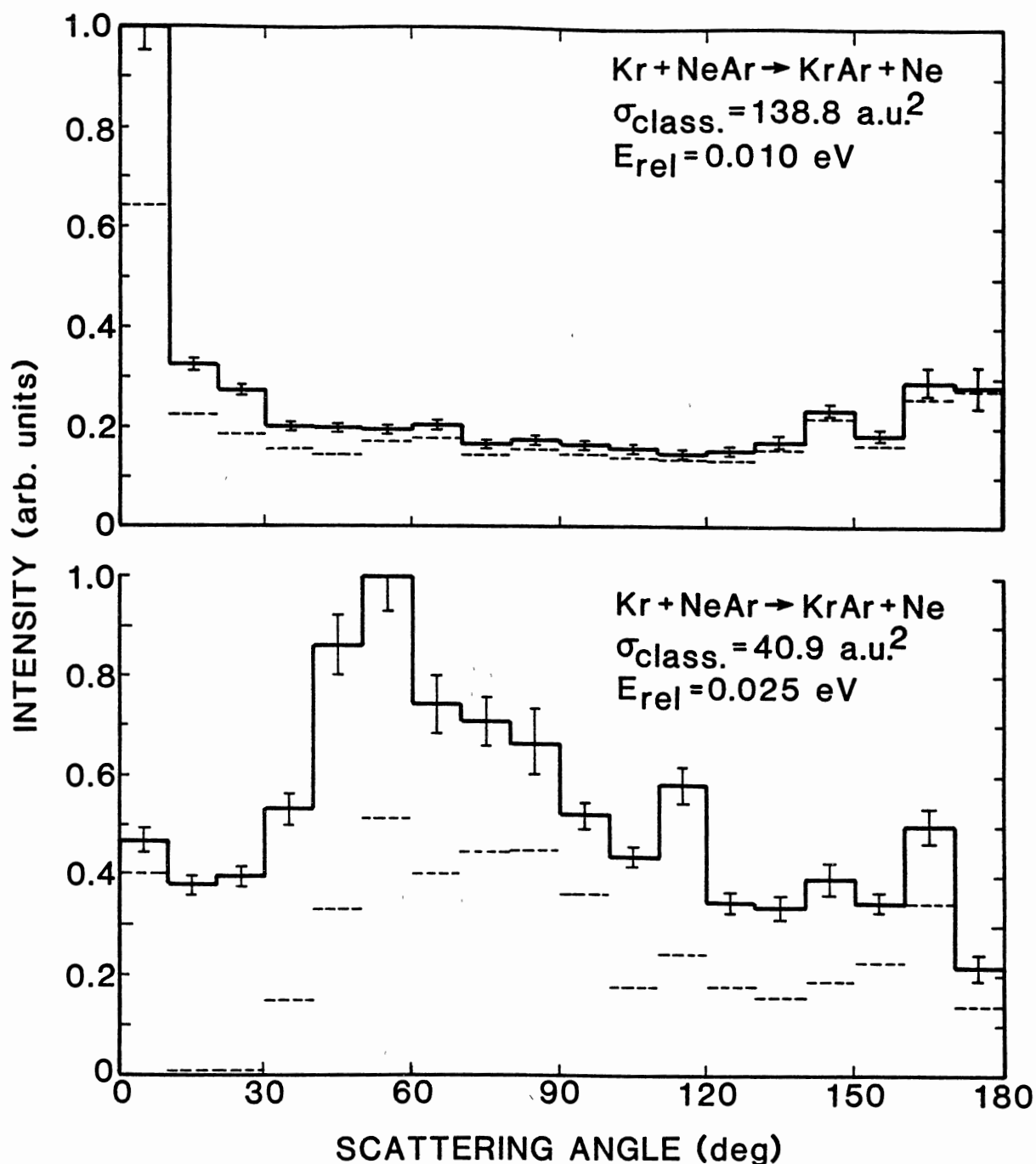


Fig. 10. Angular scattering distributions for KrAr formed by exchange in Kr + NeAr collisions at relative collisional energies of 0.010 and 0.025 eV. The solid lines are for classical intensities; the dotted lines are for tunneling-affected intensities. The total cross sections are for the classical distributions only.

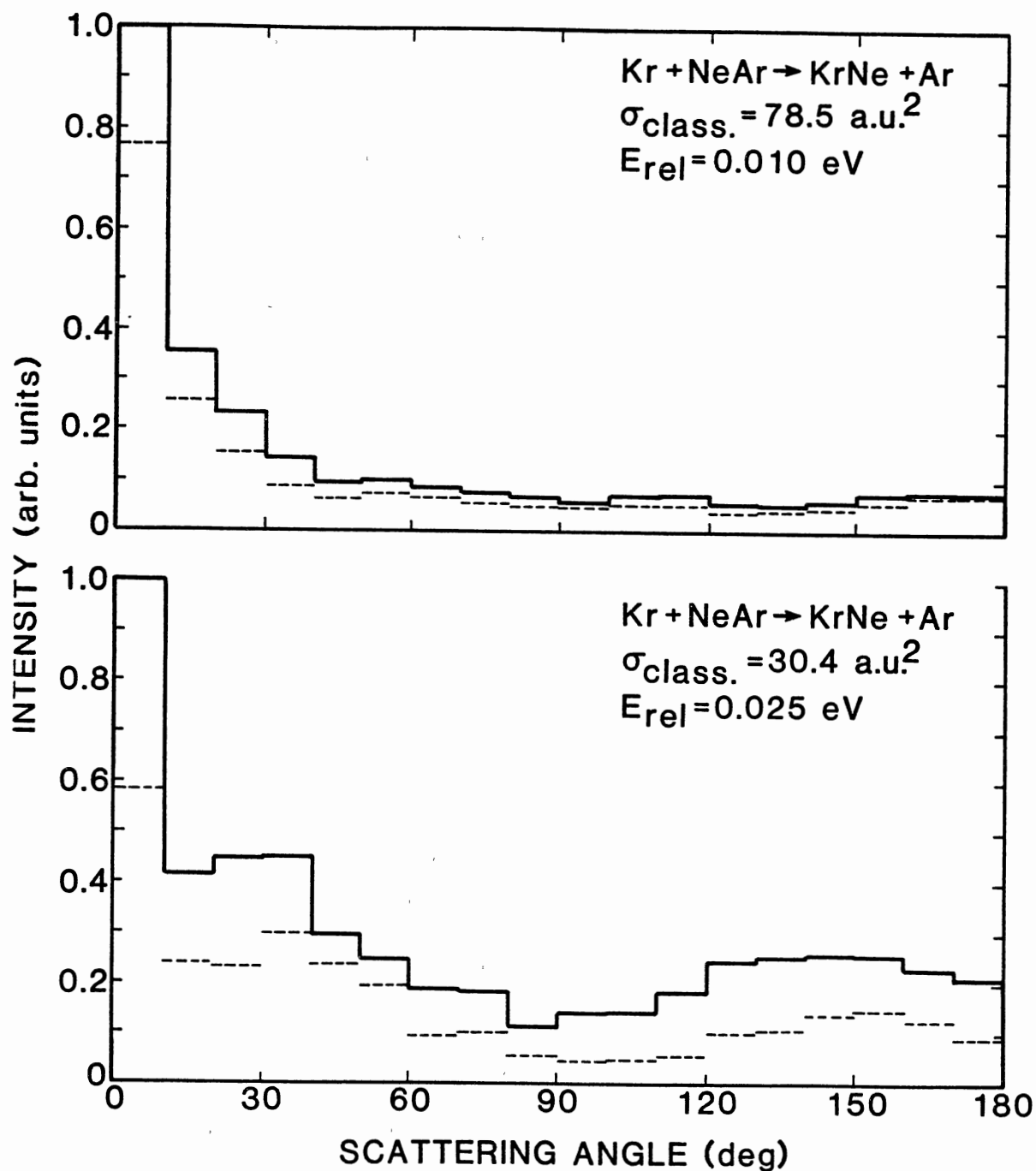


Fig. 11. Same as Fig. 10 except for KrNe exchange product.

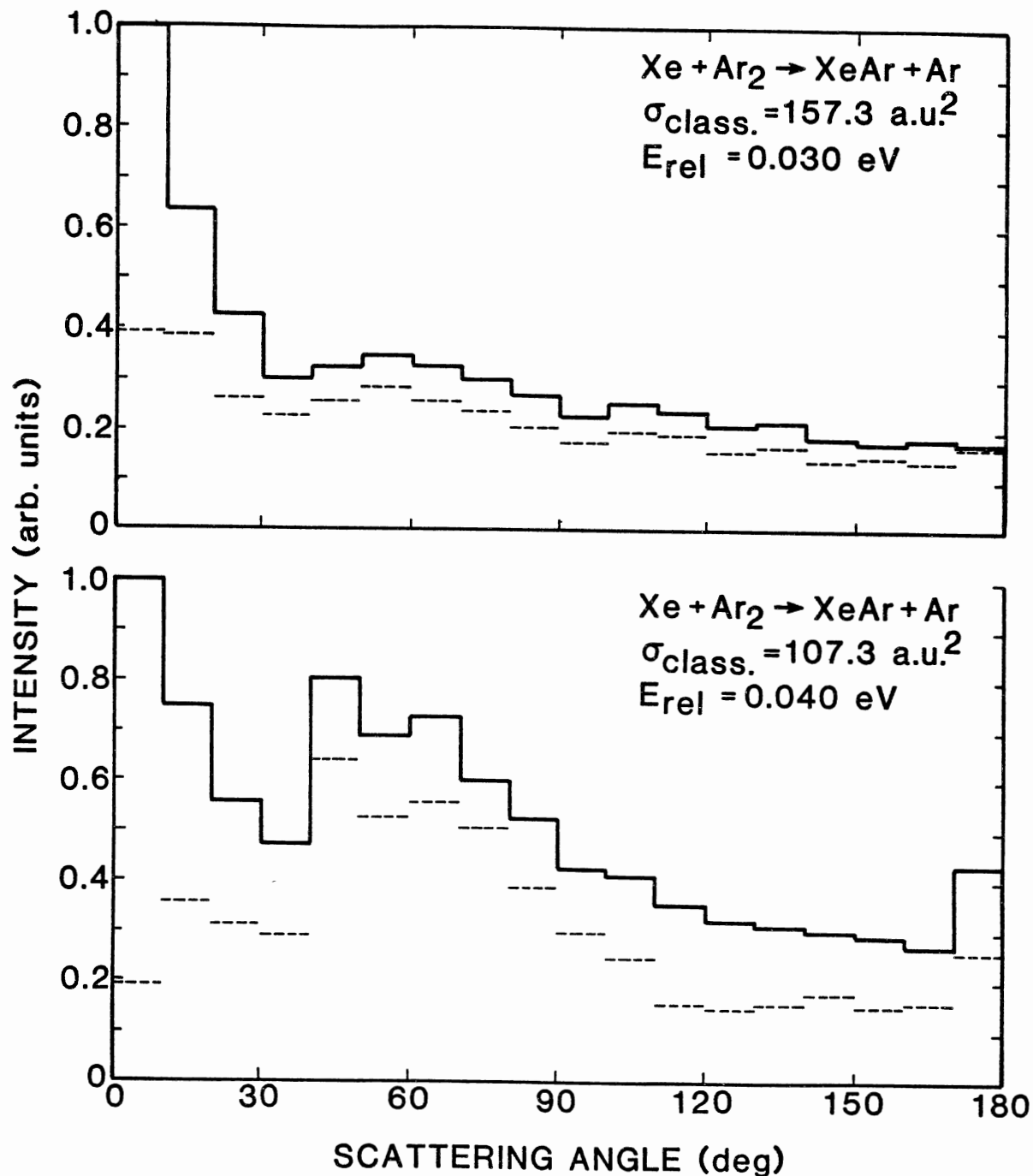


Fig. 12. Angular scattering distributions for XeAr formed by exchange in $\text{Xe} + \text{Ar}_2$ collisions at relative collisional energies of 0.030 and 0.040 eV. Plots represent the same as in Fig. 10.

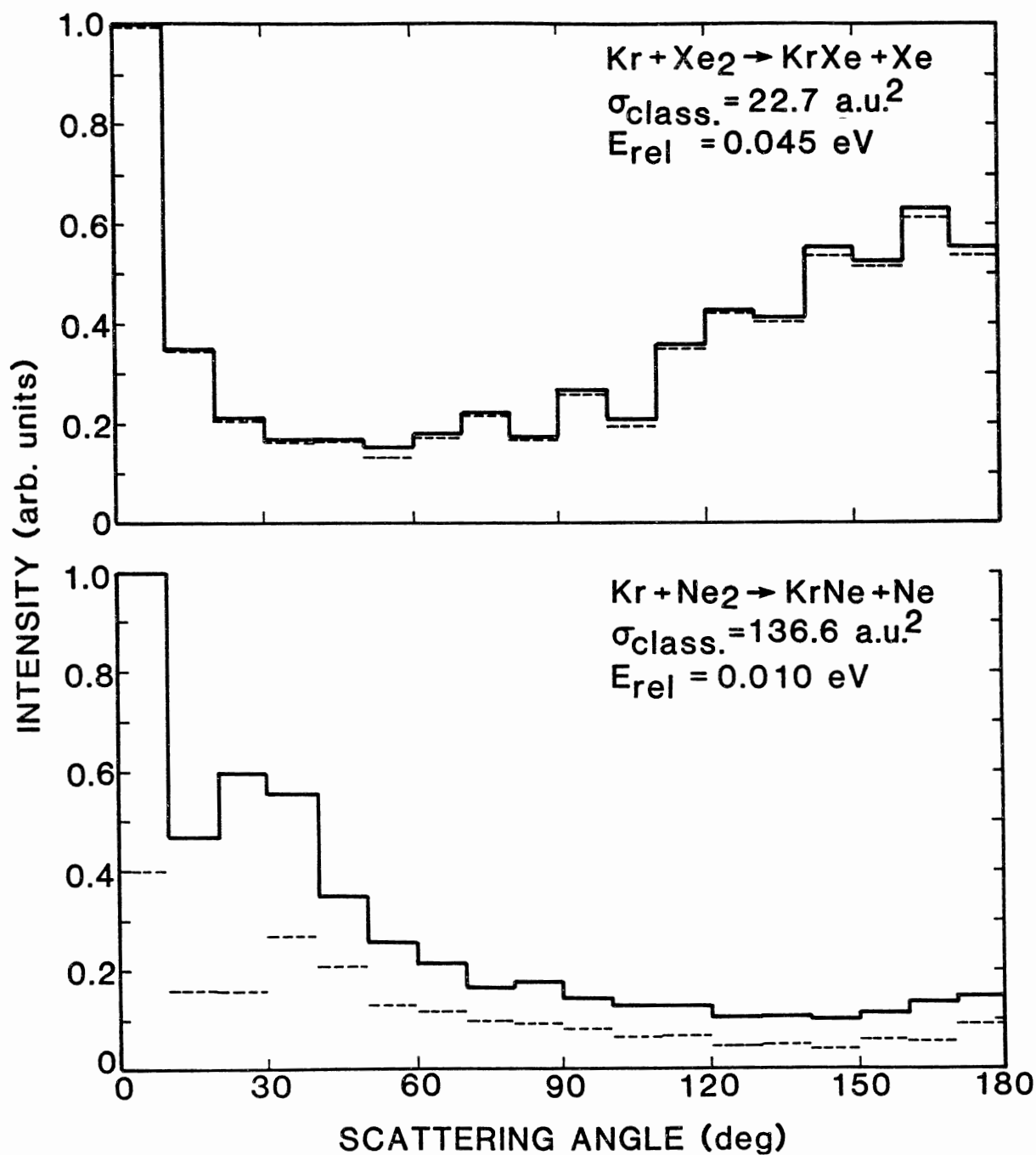


Fig. 13. Angular scattering distributions for A + BB systems. The upper graph is for Kr + Xe₂ at E_{rel} = 0.045 eV. The lower graph is for Kr + Ne₂ at E_{rel} = 0.010 eV. Plots represent the same as in Fig. 10.

results. If a metastable has a lifetime less than the computed transit time, it would dissociate before reaching the detector and is therefore not included in the intensities shown by the dotted lines in Figs. 10-13. The statistical error shown for the $\text{Kr} + \text{NeAr} \rightarrow \text{KrAr} + \text{Ne}$ reaction in Fig. 10 is typical of the error associated with all of these calculations. The magnitude of the tunneling effect is in excess of the magnitude of the statistical error.

It is not surprising to find that for all systems, at all angles, the intensities are less where dissociation of the molecules has been included. It is, however, somewhat unexpected that the tunneling corrections are relatively constant throughout all scattering angles. It might be expected that the forward scattering peaks would have larger corrections as a result of a larger population of metastables at these scattering angles. The results do not support this expectation; the percentage of metastables present is approximately the same for all scattering angles. The only exception is for $\text{Xe} + \text{Ar}_2$ at 0.030 and 0.040 eV, where the tunneling correction for forward scattered XeAr is significantly greater than that for larger scattering angles.

Angular scattering distributions at different lifetimes are given in Figs. 14-18. In all cases, the upper solid line corresponds to the intensity of stable molecules plus the intensity of metastable products having lifetimes such that they would travel at least 1 cm from the reaction site. The lower dotted lines include the intensity of all stable product dimers plus metastable dimers that travel at least 10 cm from the reaction site before dissociation. Since some of the metastables dissociate after traveling 1 cm but before traveling 10 cm, the intensity at 10 cm is less than the intensity at 1 cm. This is true for all scattering angles. Since the mean free path of the product molecules is at least 1 m in most molecular beam experiments, essentially no molecular collisions, and thus no energy transfer and subsequent dissociations occur before the product molecules travel 10 cm. Therefore, the difference between the two intensities is due strictly to tunneling of metastable dimers. Although the effect of tunneling upon intensity is obviously present, its measurement at any given single scattering angle is probably beyond the sensitivity of present-day molecular beam instruments. However, as seen in Table II, the difference between the total intensity integrated over all angles measured by a detector at 1 cm

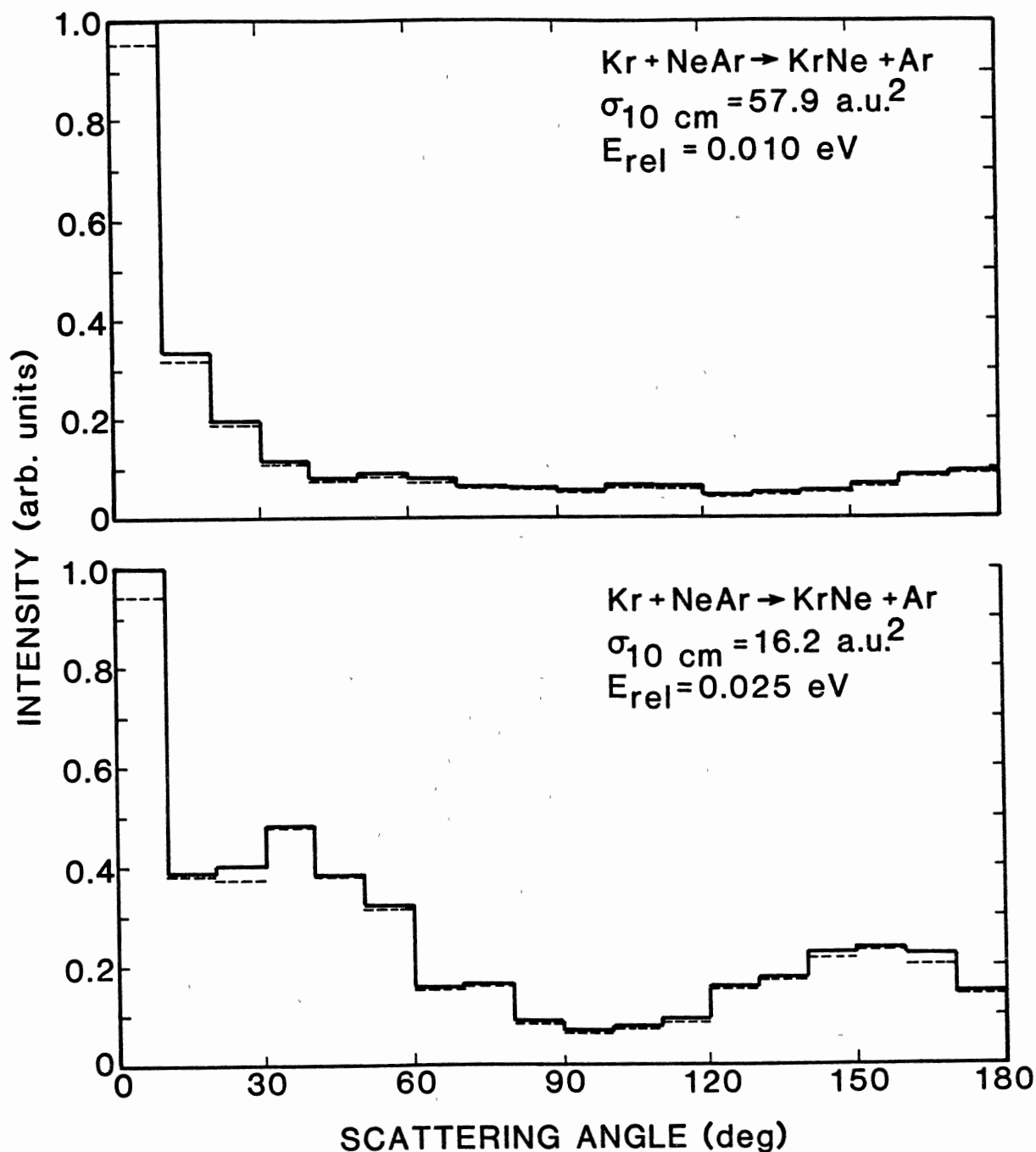


Fig. 14. Angular scattering distributions for KrNe formed by exchange in Kr + NeAr collisions at relative collisional energies of 0.010 and 0.025 eV. The solid lines represent tunneling-affected intensities at a detector 1.0 cm from the reaction site; the dotted lines represent intensities at a detector 10.0 cm from the reaction site. The total cross sections are for a detector 10.0 cm from the reaction site.

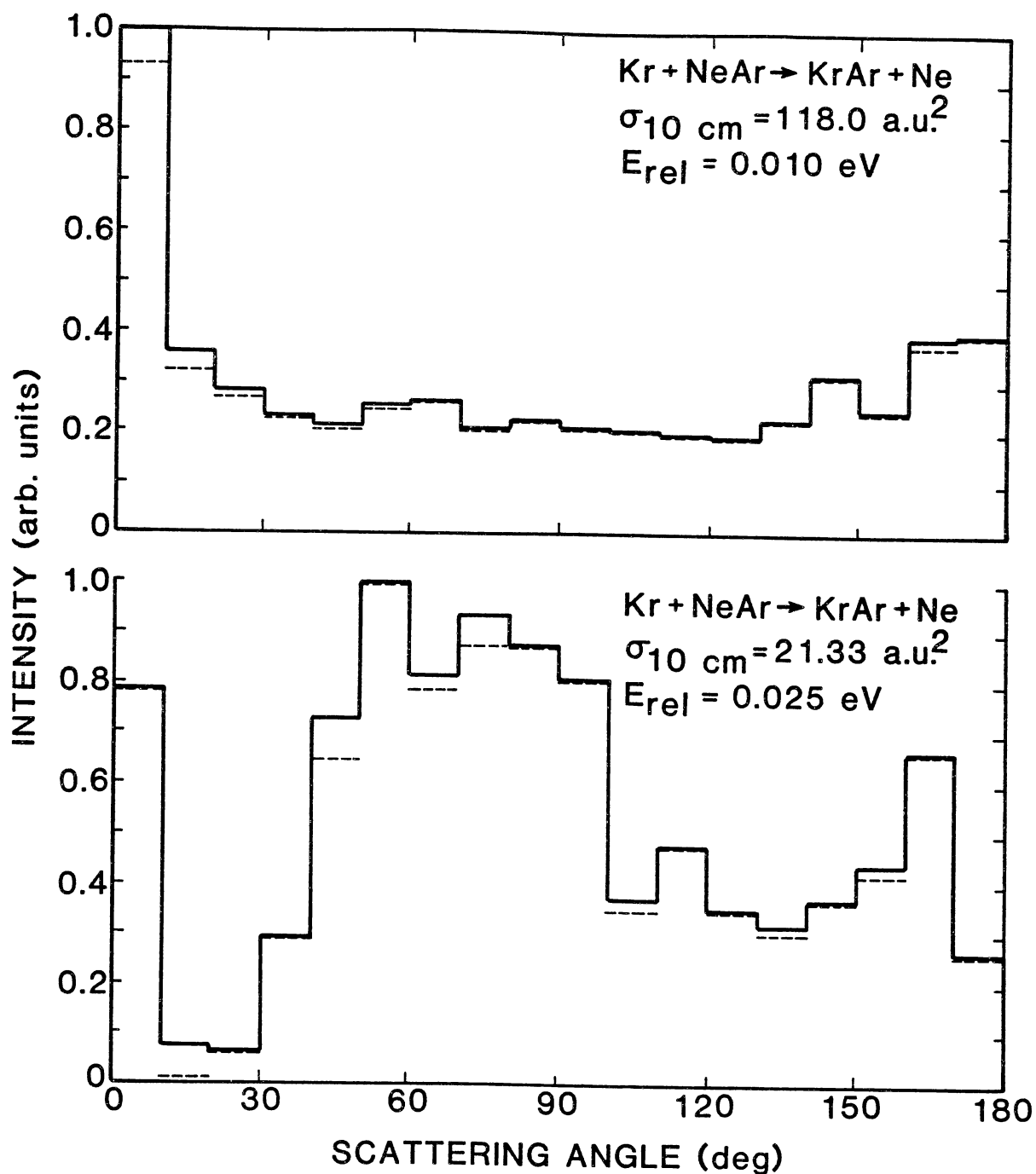


Fig. 15. Same as Fig. 14 except for KrAr exchange product.

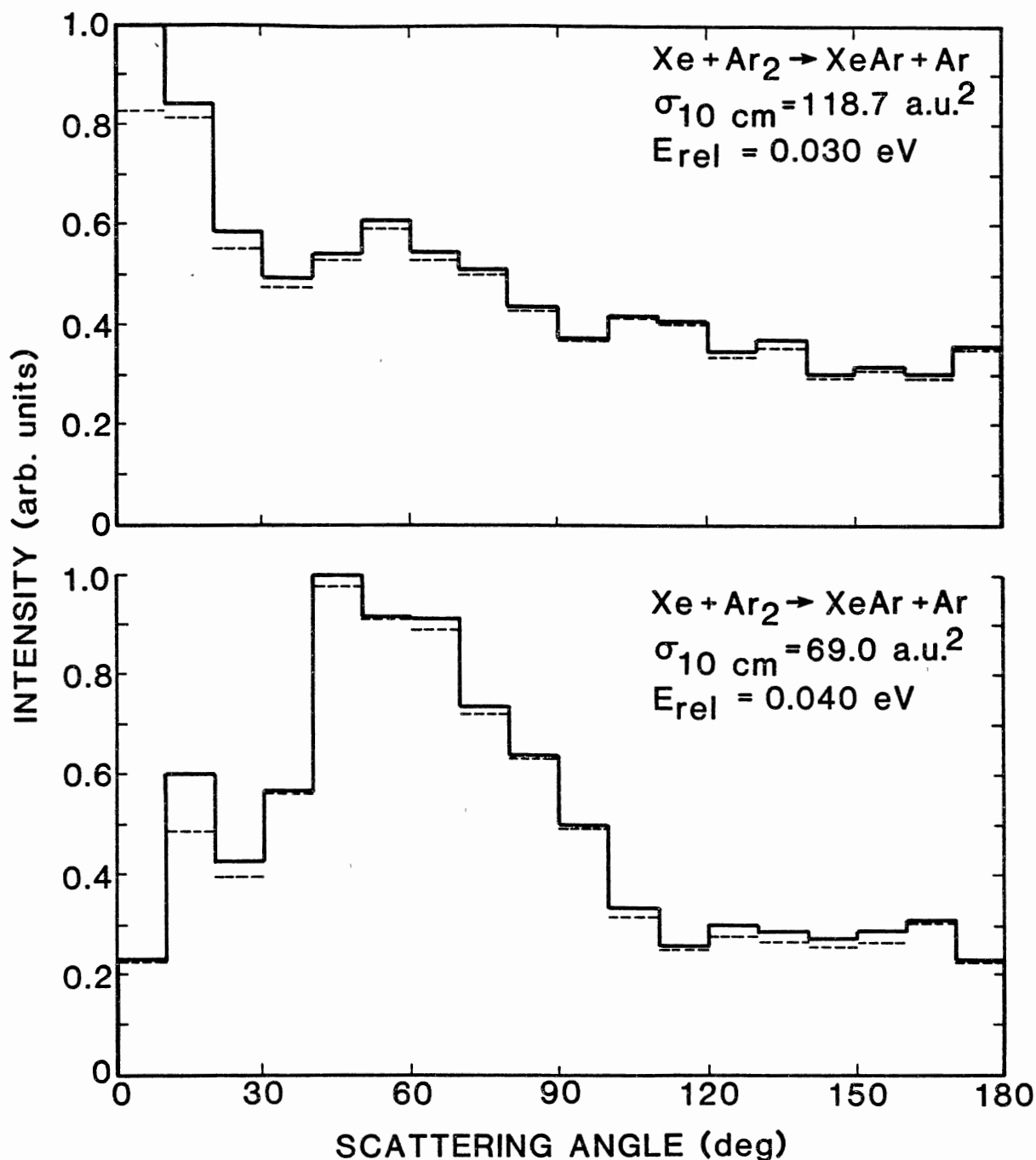


Fig. 16. Angular scattering distributions for XeAr formed by exchange in Xe + Ar₂ collisions at relative collisional energies of 0.030 and 0.040 eV. Plots represent the same as in Fig. 14.

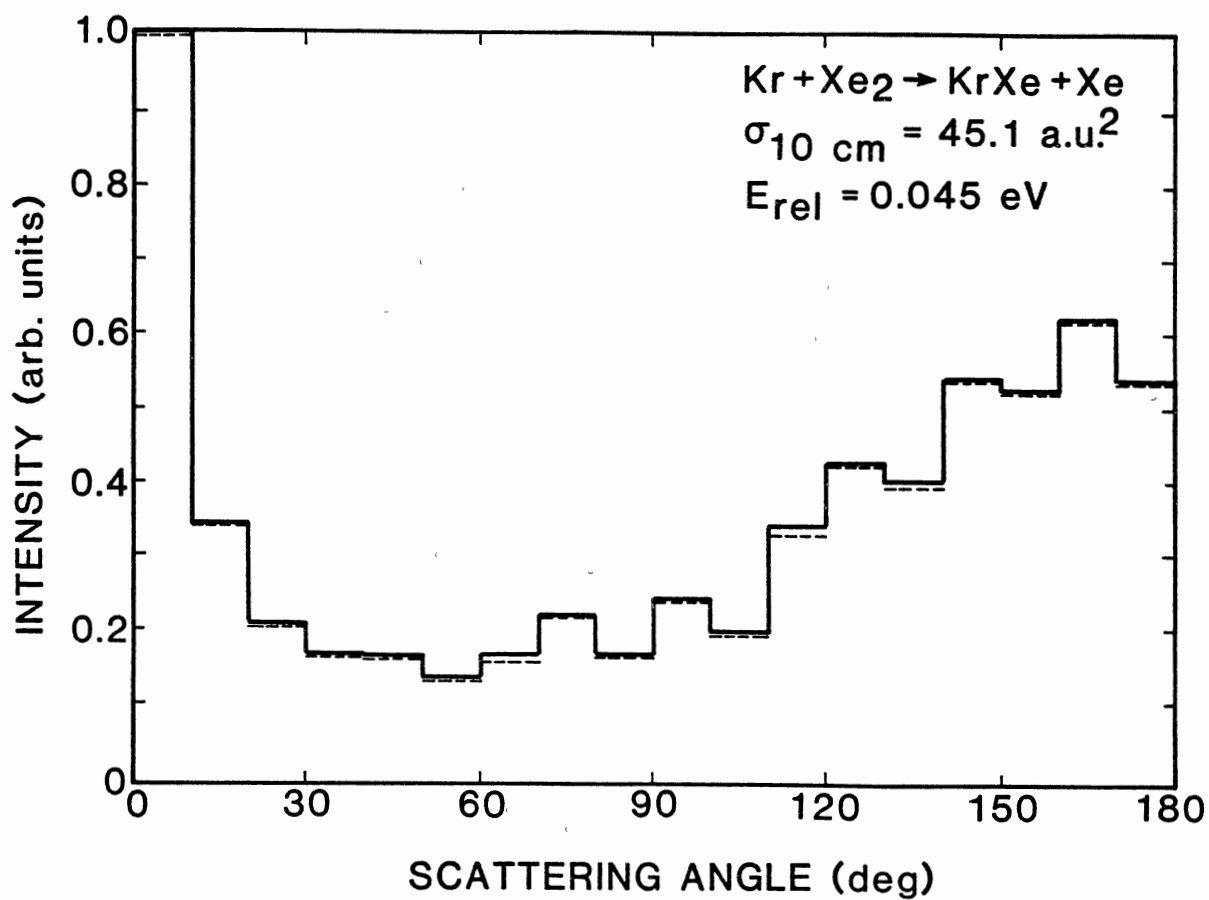


Fig. 17. Angular scattering distributions for KrXe formed by exchange in Kr + Xe₂ collisions at E_{rel} = 0.045 eV. Plots represent the same as in Fig. 14.

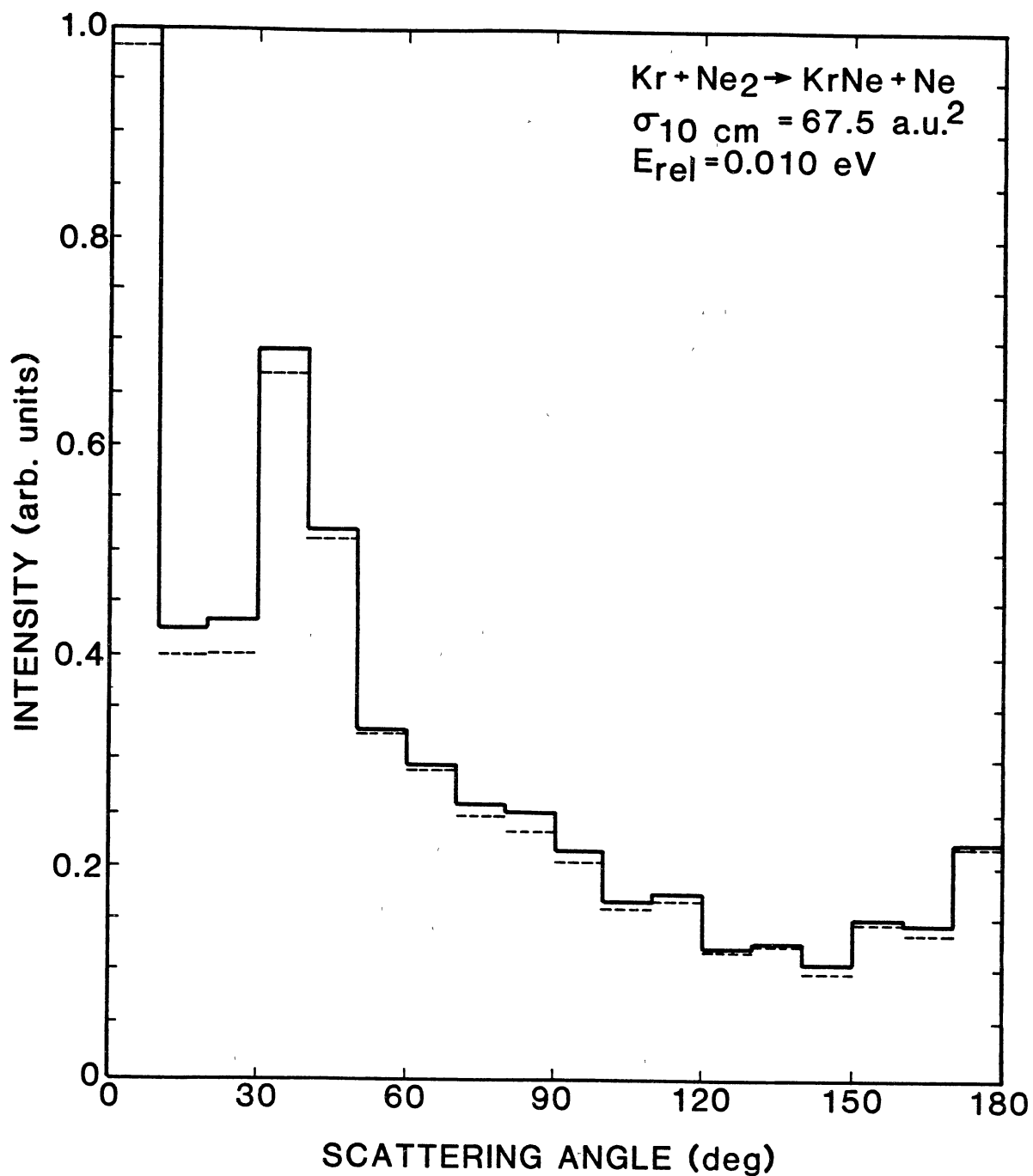


Fig. 18. Angular scattering distributions for KrNe formed by exchange in $\text{Kr} + \text{Ne}_2$ collisions at $E_{\text{rel}} = 0.010 \text{ eV}$. Plots represent the same as in Fig. 14.

and a detector at 10 cm from a crossed molecular beam reaction site is large enough that it might be measurable in a carefully designed experiment.

TABLE II. Exchange reaction cross sections as a function of relative translational energy and detector-reaction site separation for reactants in their ground vibrational and rotational states.

System	E_{rel} (eV)	(a.u. ²)	(a.u. ²)	%
		at 1.0 cm	at 10.0 cm	
Kr + NeAr \rightarrow KrNe + Ar	0.010	59.81	57.88	3.34
	0.025	16.60	16.24	2.16
Kr + NeAr \rightarrow KrAr + Ne	0.010	120.14	118.01	1.80
	0.025	22.00	21.33	3.11
Xe + Ar ₂ \rightarrow XeAr + Ar	0.030	121.73	118.73	2.52
	0.040	71.04	69.01	2.94
Kr + Xe ₂ \rightarrow KrXe + Xe	0.045	45.34	45.09	0.53
Kr + Ne ₂ \rightarrow KrNe + Ne	0.010	69.96	67.49	3.65

CHAPTER IV

CONCLUSIONS

WKB tunneling probabilities and metastable product dimer lifetimes have been computed for the $\text{Kr} + \text{NeAr}$, $\text{Kr} + \text{Xe}_2$, $\text{Xe} + \text{Ar}_2$, $\text{Kr} + \text{Ne}_2$, and $\text{Ar} + \text{Ar}_2$ systems using quasiclassical trajectories and statistical state-counting methods. Cross sections and angular scattering distributions were calculated with correction for tunneling using a WKB formalism. When these results are compared to classical distributions of the same reactions, tunneling of the metastables is found to be a significant effect. The size of the effect is dependent upon relative collisional energy, but is relatively independent of scattering angle. In a hypothetical molecular beam experiment, a difference in total integrated intensities, due solely to molecular tunneling, could possibly be measured by a variation of the detector position from 1 to 10 cm distance from the crossed beam reaction site.

BIBLIOGRAPHY

- ¹J.R. Partington, An Advanced Treatise on Physical Chemistry, (Longmans and Green, London, 1949) Vol. 1, p. 744.
- ²B.L. Blaney and G.E. Ewing, *Annu. Rev. Phys. Chem.* **27**, 533 (1976).
- ³D.L. King, D.A. Dixon, and D.R. Herschbach, *J. Am. Chem. Soc.* **96**, 3328 (1974).
- ⁴D.L. Thompson and L.M. Raff, *J. Chem. Phys.* **76**, 301 (1982).
- ⁵L.M. Raff and D.L. Thompson, *J. Chem. Phys.* **77**, 6065 (1982).
- ⁶D.R. Worsnop, J.J. Buelow, and D.R. Herschbach, *J. Phys. Chem.* **85**, 3024 (1981).
- ⁷(a)M. Yamashita, T. Sano, S. Kotake, and J.B. Fenn, *J. Chem. Phys.* **75**, 5355 (1981). (b)R. Viswanathan, L.M. Raff, and D.L. Thompson, *ibid.* **79**, 2857 (1983).
- ⁸L.M. Raff and D.L. Thompson, in Theory of Chemical Reaction Dynamics, edited by M. Baer (Chemical Rubber Company, Cleveland, 1984).
- ⁹C.Y. Ng, Y.T. Lee, and J.A. Barker, *J. Chem. Phys.* **61**, 1996 (1974).
- ¹⁰R.J. LeRoy, *J. Chem. Phys.* **57**, 573 (1972).
- ¹¹R.A. Aziz, J. Presley, U. Buck, and J. Schleusener, *J. Chem. Phys.* **70**, 4737 (1979).
- ¹²G. Scoles, *Annu. Rev. Phys. Chem.* **31**, 81 (1980).
- ¹³R.T. Pack, J.J. Valentini, C.H. Becker, R.J. Buss, and Y.T. Lee, *J. Chem. Phys.* **77**, 5475 (1982).
- ¹⁴J.A. Barker, R.O. Watts, J.K. Lee, T.P. Schafer, and Y.T. Lee, *J. Chem. Phys.* **61**, 3081 (1974).

¹⁵J.M. Farrar, T.P. Schafer, and Y.T. Lee, AIP Conf. Proc. No. 11, 279 (1973).

(2)

VITA

Randy Allen Turner

Candidate for the Degree of
Master of Science

Thesis: A. AN AB INITIO STUDY OF $\text{Li}_2[\text{CO}_3]$ AND $\text{Na}_2[\text{CO}_3]$
ION TRIPLETS

B. THEORETICAL STUDIES OF TUNNELING PROCESSES
IN THREE-BODY EXCHANGE REACTIONS OF VAN
DER WAALS RARE GAS DIMERS

Major Field: Physical Chemistry

Biographical:

Personal Data: Born in Okinawa, January 12, 1956,
the son of Maj. Edward B. and Juanita M.
Turner. United States citizen by military
parents overseas.

Education: Graduated from Richfield High School,
Waco, Texas, in May 1974; received Bachelor of
Science Degree in Chemistry, Physics, and
Mathematics from Baylor University, Waco,
Texas, in May 1980; completed requirements for
Master of Science Degree in Physical Chemistry
at Oklahoma State University in May 1990.

Professional Experience: Graduate Teaching
Assistant and/or Graduate Research Assistant,
Department of Chemistry, Oklahoma State Uni-
versity, August 1980 to August 1986; summer
intern at AMOCO Research Center, Naperville,
Illinois, summer of 1981.

Publications: Randy A. Turner, L.M. Raff, and
D.L. Thompson, J. Chem. Phys. 80, 3189 (1984).